

Spring 5-2017

Structural Design of a Business Jet Winglet

Jaime Gutierrez
Embry-Riddle Aeronautical University

Follow this and additional works at: <https://commons.erau.edu/edt>



Part of the [Aeronautical Vehicles Commons](#)

Scholarly Commons Citation

Gutierrez, Jaime, "Structural Design of a Business Jet Winglet" (2017). *Doctoral Dissertations and Master's Theses*. 333.

<https://commons.erau.edu/edt/333>

This Thesis - Open Access is brought to you for free and open access by Scholarly Commons. It has been accepted for inclusion in Doctoral Dissertations and Master's Theses by an authorized administrator of Scholarly Commons. For more information, please contact commons@erau.edu.

STRUCTURAL DESIGN OF A BUSINESS JET WINGLET

A Thesis

Submitted to the Faculty

of

Embry-Riddle Aeronautical University

by

Jaime Gutierrez

In Partial Fulfillment of the

Requirements for the Degree

of

Master of Science in Aerospace Engineering

May 2017

Embry-Riddle Aeronautical University

Daytona Beach, Florida

STRUCTURAL DESIGN OF A BUSINESS JET WINGLET

by

Jaime Gutierrez

A Thesis prepared under the direction of the candidate's committee chairman, Dr. Luis Gonzalez, Department of Aerospace Engineering, and has been approved by the members of the thesis committee. It was submitted to the School of Graduate Studies and Research and was accepted in partial fulfillment of the requirements for the degree of Master of Science in Aerospace Engineering.

THESIS COMMITTEE



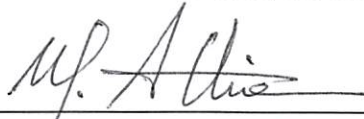
Chairman, Dr. Luis Gonzalez



Member, Dr. Daewon Kim



Member, Dr. Sirish Namilae



Graduate Program Coordinator, Dr. Magdy Attia

5/31/2017
Date



Dean of College of Engineering, Dr. Maj Mirmirani

5/31/2017
Date



Vice Chancellor, Academic Support, Dr. Christopher Grant

5/31/2017
Date

ACKNOWLEDGMENTS

I would first like to express my sincere gratitude to my thesis advisor Dr. Gonzalez for steering me in the right direction whenever it was necessary. His patience, knowledge, and enthusiasm pushed me to finish my work.

I would also like to thank Donald Pointer, Lionel De La Sayette, and Michel Lavanant, from Dassault Falcon Jet and Dassault Aviation, and Dean Dr. Mirmirani who provided guidance regularly.

I also like to acknowledge Dassault Aviation, Dassault Falcon Jet, and Embry-Riddle Aeronautical University for their financial support.

I also wish to thank my committee members, Dr. Kim and Dr. Namilae, for their valuable comments.

Finally, I must express my very profound gratitude to my parents for their un-failing support throughout my studies. This accomplishment would not have been possible without them.

TABLE OF CONTENTS

	Page
LIST OF TABLES	vi
LIST OF FIGURES	vii
SYMBOLS	x
ABBREVIATIONS	xi
ABSTRACT	xii
1 Introduction	1
1.1 Background	1
1.2 Scope	3
1.3 Winglet Structures Research	3
2 FAA Regulations	6
2.1 Critical Load Conditions	6
3 Methodology	9
3.1 Current Wing Structural Arrangement	9
3.2 Design Concepts	11
3.3 Material Selection	13
3.3.1 Selected Material	15
3.3.2 Honeycomb Material	20
3.4 Analysis Tools	21
3.5 Loads Development	22
3.5.1 Shear and Moment Diagrams	24
3.5.2 Torsion Diagram	26
3.6 Finite Element Analysis	27
3.6.1 Element Type	27
3.6.2 Load Application	29
3.6.3 Mesh Independence Study	30
3.7 Static Analysis	33
3.8 Buckling Analysis	34
4 Results and Discussion	35
4.1 Ultimate Load	36
4.2 Limit Load	42
4.3 Buckling	47

	Page
5 Fabrication	49
5.0.1 Fasteners	51
5.1 Winglet Assembly	52
5.2 Connection to the Wing	53
5.2.1 Corrosion Prevention	53
5.3 Weight Estimation	54
6 Conclusion and Future Work	56
REFERENCES	58
A Engineering Drawings	61

LIST OF TABLES

Table	Page
1.1 Falcon 10 operating weights.	2
2.1 Flight conditions.	8
3.1 Material selection summary.	19
3.2 Honeycomb material properties.	21
4.1 Final design thicknesses.	35
4.2 Stress at negative sideslip load.	36
4.3 Stress at positive sideslip load.	37
4.4 Stress at gust load.	37
4.5 Shear stress on the bolts.	40
4.6 Stress at negative sideslip load.	42
4.7 Stress at positive sideslip load.	43
4.8 Stress at gust load.	43
4.9 Eigenvalue buckling with negative sideslip load.	47
5.1 Bolt dimensions.	51
5.2 NAS1739B-4-04 rivet dimensions.	52
5.3 Weight summary.	55

LIST OF FIGURES

Figure	Page
1.1 Falcon 10 dimensions.	2
1.2 Winglet dimensions.	3
1.3 Examples of winglet structures.	4
2.1 FBD Gust Condition	7
3.1 Falcon 10 wing structure.	10
3.2 Falcon 10 wing tip.	10
3.3 Ashby plot with conflictive objectives for the spar material.	16
3.4 Ashby plot with conflicting objectives for the upper skin panel.	17
3.5 Ashby plot with conflicting objectives for the lower skin panel.	18
3.6 Strength comparisson.	19
3.7 Positive Angles.	22
3.8 Reference plane.	23
3.9 Normal pressure.	23
3.10 Shear diagram.	24
3.11 Moment diagram.	25
3.12 Torsion diagram.	26
3.13 Shell Element.	27
3.14 Solid Element.	28
3.15 Beam Element.	29
3.16 Pressure load on winglet.	30
3.17 Spider web connection between spars.	30
3.18 Mesh independence with gust load.	31
3.19 Mesh independence with positive sideslip.	31
3.20 Mesh independence with negative sideslip.	32

Figure	Page
3.21 Failure map of a rectangular beam with honeycomb.	34
4.1 Maximum principal stress at ultimate load.	38
4.2 Minimum principal stress at ultimate load.	39
4.3 Bolt numbering.	41
4.4 Shear stress per bolt.	41
4.5 Maximum principal stress at limit load.	44
4.6 Minimum principal stress at limit load.	45
4.7 Equivalent von-Misses stress at limit load.	46
4.8 First mode buckling shapes.	48
5.1 Bill of Materials.	50
5.2 MS24694 bolt dimensions.	51
5.3 NAS1739B-4-04 rivet dimensions.	52
A.1 3 view drawing	61
A.2 Rib 17	62
A.3 Rib 18	63
A.4 Slat Cover	64
A.5 Aileron Cover	65
A.6 Front spar	66
A.7 Rear spar	67
A.8 Honeycomb sandwich	68
A.9 Leadin edge A	69
A.10 Leading edge B	70
A.11 Top inspar skin	71
A.12 Bottom inspar skin	72
A.13 Top middle skin	73
A.14 Top middle skin	74
A.15 Bottom middle skin	75
A.16 Bottom middle skin	76

A.17 Navigation light cover 77

SYMBOLS

C_L	lift coefficient
E	Young's Modulus
K_g	gust correction factor
n	load factor
S	wing surface area
σ_c	compressive strength
σ_t	tensile strength
σ_y	yield strength
σ_u	ultimate strength
U_e	gust speed
V_{eq}	equivalent speed
W	weight
α	angle of attack
β	sideslip angle
ρ_{SL}	air density at sea level
Ω	distance from winglet root

ABBREVIATIONS

a.c.	Aerodynamic center
CFD	Computational Fluid Dynamics
FAA	Federal Aviation Administration
FAR	Federal Aviation Regulation
FEA	Finite Element Analysis
MS	Margin of Safety
NS	Negative Sideslip
PS	Positive Sideslip
SCC	Stress-Cracking Corrosion

ABSTRACT

Gutierrez, Jaime MSAE, Embry-Riddle Aeronautical University, May 2017. Structural Design of a Business Jet Winglet.

Structural sizing of a winglet for the Falcon 10 was performed and is presented here. The aerodynamic profile of the winglet was taken from a previous study, which predicted an increase in range of 3.3% with an estimated weight increase of 52 kg. An investigation of the current structure layouts and materials used in the industry was conducted. Six loading cases were analyzed to identify the most critical for the winglet, found to be negative and positive sideslip and gust. A finite element model was developed and used to size the structure. A fabrication process and assembly is described and the weight was estimated to be 22.5 kg which is less than the estimated weight. Thus the performance of the aircraft will be increased.

1. Introduction

1.1 Background

The performance enhancement that winglets achieve has been proven since they were first commercially introduced by Whitcomb in the mid-1970's (Whitcomb, 1976). Winglets are extensions to the wing which reduce the induced drag by decreasing the intensity of the wing tip vortex. New aircraft models include winglets in their design, while older aircraft can be retrofitted. Winglets have been used as a relatively inexpensive method to increase the performance of aging airline's aircraft fleets. The business jet sector of aviation has benefited from the use of winglets due to the resulting increase in range and climb speed, as well as the improved aesthetics of older aircraft. Business jet manufacturing companies such as Dassault Falcon have implemented winglets in their designs, in addition to retrofitting older versions of their aircraft such as the Falcon 900 and 2000.

The aircraft of interest in this study is the Falcon 10 which entered service in 1973 and has a capacity of 4-8 passengers. Its maximum operating Mach number is 0.87 and it has a ceiling of 45,000 ft. In terms of performance, it is capable of flying for 2,000 NM with four passengers at 35,000 ft, at a speed of M0.75 (Avions Marcel Dassault Technical Report, 1972). The aircraft's dimensions are presented in Fig. 1.1 and its operating weights are given in Table 1.1.

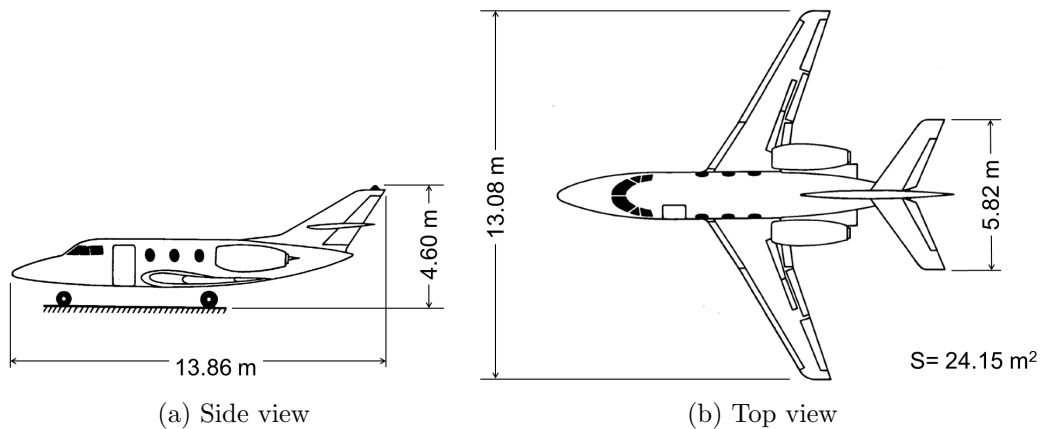


Figure 1.1: Falcon 10 dimensions.

The work presented here is the continuation of previous research. The winglet geometry and performance calculations, as well as the structural reinforcement of the wing were performed by El Haddad (2015). The final aerodynamic profile and dimensions are shown in Fig. 1.2. The winglet has a toe out angle of 2 deg and a leading edge sweep of 40 deg. A total of 12 candidates were analyzed to achieve the optimum consisting of induced drag reduction not offset by the necessary profile drag and structural weight increases. The final winglet proposed resulted in a range increase of 3.3% and fuel reduction of 3.8% for the Falcon 10 on a 1,200 NM mission

Table 1.1: Falcon 10 operating weights.

Max. takeoff weight	18,300 lb
Max. zero fuel weight	12,460 lb
Min. weight	9,920 lb
Typical empty weight	11,460 lb

(El Haddad, 2015). The performance calculations were carried out with an estimated winglet weight of 52 kg.

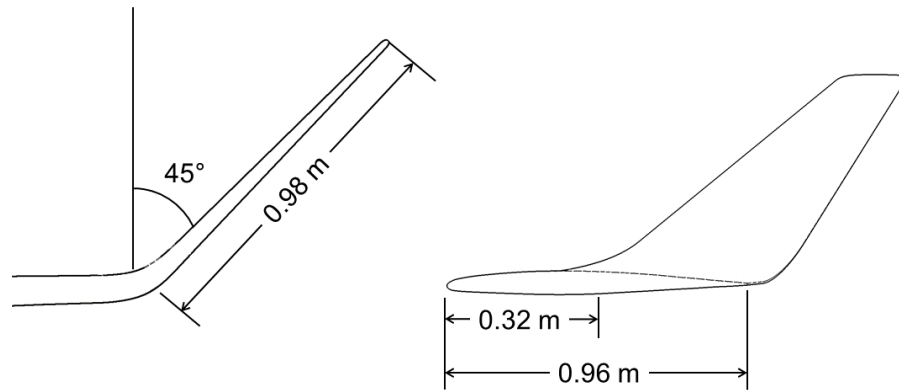


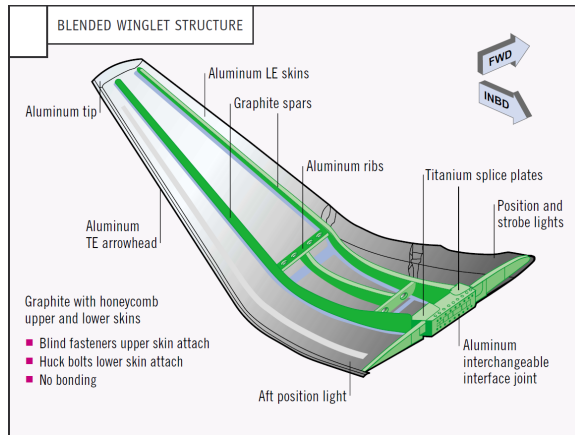
Figure 1.2: Winglet dimensions.

1.2 Scope

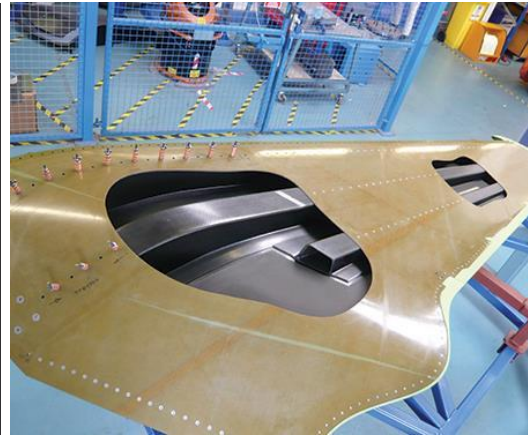
The goal of this study is to perform the structural sizing of the winglet for the Falcon 10 proposed by El Haddad (2015). In order to attain or increase its previously estimated performance, the total weight of the winglet must be equal to or less than 52 kg. The estimated weight includes the weight of the fasteners.

1.3 Winglet Structures Research

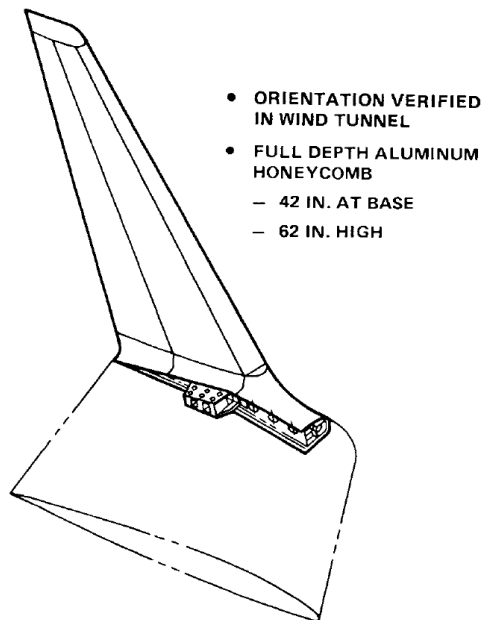
Research was carried out to gain insight into current structural design of winglets used in the industry. This study focused on identifying the methods of connection between the wing and the winglet, the internal structure, and the materials used.



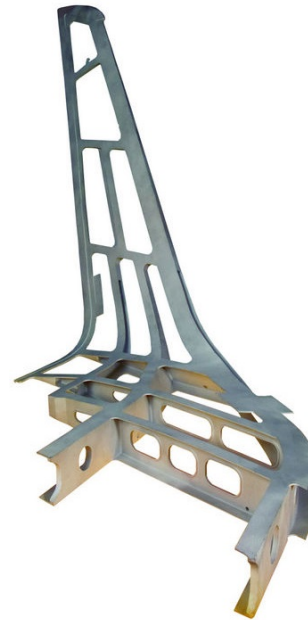
(a) Boeing 737-800 (Faye et al., 2002)



(b) GKN design with co-cured upper skin and waffle stiffener ("GKN Leads "STeM" Program to Successful Conclusion")



(c) Gulfstream GII (Mead et al., 1980)



(d) Aeromet A20X cast winglet ("Aeromet International LTD", n.d.)

Figure 1.3: Examples of winglet structures.

Early winglet designs used metallic materials, whereas more modern ones have resorted to composites (Whitcomb, 1976; Faye et al., 2002). For example, the Gulfstream GII winglets (Fig. 1.3) had a metallic structure, no cant, and their connection

to the wing was done by using a strong fitting that transfers the load to the skin and then to a full-depth honeycomb. Later designs use a combination of metals and composites, for example, the B737-800 blended winglet. The study observed that the use of composite materials eliminates the need for a full-depth honeycomb because the skin is capable of carrying more load.

The type of connection to the wing tends to depend on the available depth of the cross-section. For larger winglets, such as those installed on the KC135, B737-800, and A320NEO, lug fittings are used. This configuration consists of a lower lug that reacts axial and vertical loads and an upper lug which resists axial loads. This attachment method can be used in wing tips where enough space is available to accommodate the lugs and results in relative ease of manufacturing.

2. FAA Regulations

All structural elements in an aircraft must comply with the federal regulations. The FAR Part 25 subpart C specifies the guidelines for proving the structural airworthiness of the aircraft and imposes requirements on the structure with regards to limit and ultimate loads. The limit load is defined as the maximum load expected during service, and the ultimate load is the limit load multiplied by a factor of safety. The factor of safety is specified to be 1.5, as per FAA Part 25.303. The following section describes the guidelines implemented to determine the load conditions for which the structure will be sized.

2.1 Critical Load Conditions

The load cases for which the structures are sized depend on the location and type of the structure of interest. Sideslip and gust flight conditions are critical cases for the winglet (Whitcomb, 1976). The gust condition can be estimated by using a simple mathematical model that assumes a sharp-edged vertical gust, as seen in Fig. 2.1, where the gust has a speed, U_e , that increases the angle of attack without affecting the aircraft's airspeed (Torenbeek and Wittenberg, 2009). However, the assumption of the sharp rise is not realistic and, therefore, a correction factor, K_g , is used to simulate a smoother transition. This factor is a function of the aircraft weight and

geometry. The flight conditions at which gust is most critical to the winglet were calculated with Eq. 2.1. The gust speed value of 7.5 m/s, suggested Torenbeek and Wittenberg (2009), was used for the calculations, and the load factor was taken from a structures report on the Falcon 10 by Dassault (Avions Marcel Dassault-Breguet Aviation, 1972).

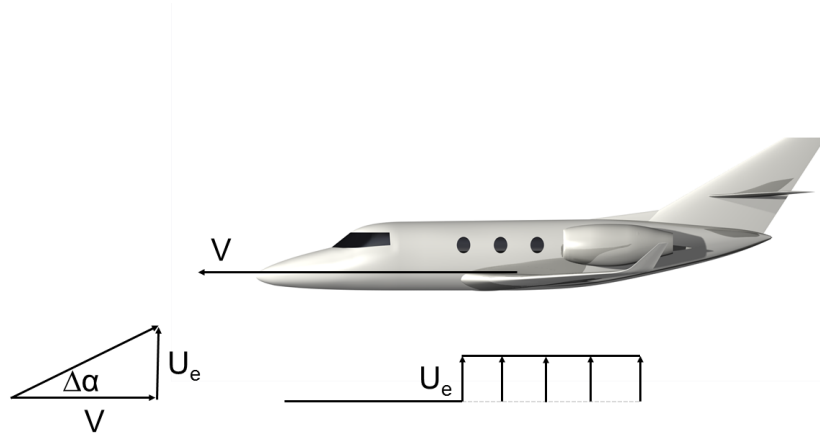


Figure 2.1: Increase of angle of attack due to gust (Torenbeek and Wittenberg, 2009).

Other loads taken into consideration include roll, which is critical for the outboard section of the wing (Faye et al., 2002). In this case the aircraft experiences a load factor of two, which corresponds to a 60 deg bank. Level flight at different load factors was also investigated. The summary of the flight load conditions is shown in Table 2.1. These values were then used to calculate the aerodynamic loads to be applied in the finite element model for sizing the winglet structure.

$$n = 1 + K_g \frac{dC_L}{d\alpha} \frac{\rho_{sl} U_e V_{eq}}{2W/S} \quad (2.1)$$

Table 2.1: Flight conditions

Flight condition	Load factor	Altitude (ft)	Velocity	Attitude
Level flight	3	18,000	M0.80	$\alpha = 2$ deg
Gust	5	23,000	M0.84	$\alpha = 8$ deg
Sideslip	3	19,000	MMO (M0.87)	$\beta = \pm 16.5$ deg
Roll	2	10,000	$V_A(220K_{EAS})$	$\theta = \pm 60$ deg

3. Methodology

The design of the winglet structure and wing tip attachment is described in the following sections. First, a preliminary layout of the structure was created. A CAD model was created in CATIA to establish the winglet dimensions and to assess the type of structure that could be implemented, given the available space. The layouts generated incorporated considerations for winglet attachment and for ease of installation.

The following sections give a general description of the current wing structure and of the investigated winglet design concepts.

3.1 Current Wing Structural Arrangement

The Falcon 10 wing structure conforms to a conventional wing design. As illustrated in Fig. 3.1, the principal structure constitutes a wing box comprised of a front and a rear spar with upper and lower skins and 16 ribs. The spars end at rib 16, where the wing tip fairing is attached.

The spars have a C-channel cross-section with tapered thickness. At the end of the wing box, the front and rear spars thicknesses are 1.8 and 2.0 mm, respectively. The spar caps also reduce in thickness as they span out, and their thickness at the end of the wing box is 4.7 mm.

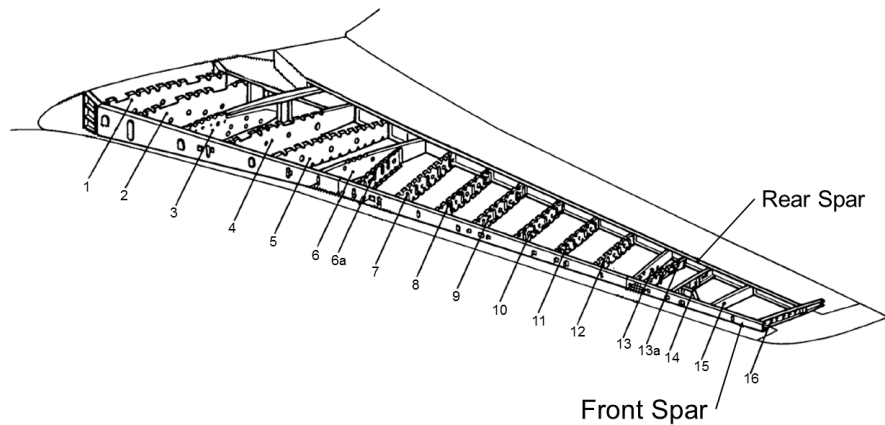


Figure 3.1: Falcon 10 wing structure.

The wing tip is attached to the wing box via rib 16. The left wing tip structure can be seen in Fig. 3.2, which shows the attachment of the small spars to rib 16 at the same location where the wing front and rear spars are attached to the rib.

All Falcon aircraft feature inboard and outboard slats. The Falcon 10 outboard slats go up to the wing tip. The ailerons are attached to the rear spar and extend up to rib 17. The current structural wing layout was taken into consideration for the winglet-to-wing connection layout.

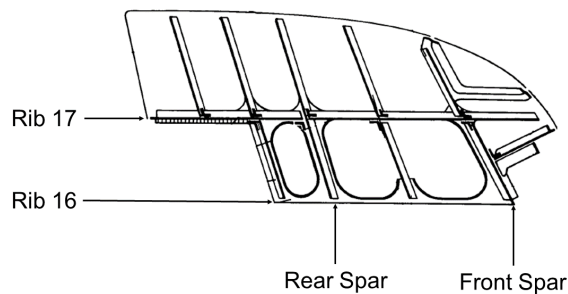


Figure 3.2: Falcon 10 wing tip.

3.2 Design Concepts

Two structure layouts were considered. The first consists of two spars, one connected to the wing's rear spar and continuing straight throughout the span of the winglet. The winglet front spar would be a kinked spar connected to the wing box at the wing front spar. This concept was eventually discarded because of the size constraint, which could complicate manufacturing. The complexity of installation of the kinked front spar would also complicate manufacturing because of the large leading edge sweep of the aerodynamic profile.

The other design considered consists of one spar connected to the wing's rear spar. The connection to the wing is made with a stub spar connected to the wing rear spar to provide axial and vertical load resistance. The upper and lower skin connections react the axial loads. The spar continues along the thickest section of the winglet up to a rib. From that point on to the winglet tip, a full-depth honeycomb is sufficient to carry the load. The wing's front spar is used to attach a short spar that alleviates the loading in the connection at the rear spar. The use of honeycomb makes the skin effective in providing bending and torsional stiffness.

The initial sizing of the rear spar cap cross-section was performed by following the method suggested by Anderson (1999), in which Eq. 3.1 is used. There, A is the spar cap area, M is the maximum bending moment, d is the distance between centroids of the caps, and σ_y is the allowable stress.

$$A = \frac{M}{d \sigma_y} \quad (3.1)$$

The maximum bending moment was taken from the diagram in section 3.5.1, and the allowable stress was taken from the yield stress of section 3.3.1 divided by the factor of safety. This yields a spar cap area of 112 mm².

The spar attachment arrangement was determined following the considerations presented by Niu (1999). The distance from the center of the fastener to the edge of the structure is given by Eq. 3.2, where r is the hole diameter and d is the distance from the edge to the center of the hole. The bolt diameter was determined by taking the height of the shorter spar and using Eq. 3.2 to calculate the maximum allowable fastener diameter. The fastener spacing was taken as four times the diameter.

$$d = 4r + 1.52 \text{ mm} \quad (3.2)$$

Other factors considered included the diameter of the rivet and how it relates to the skin thickness. For fatigue critical connections, the relationship between the sheet thickness and the rivet's height, h , is given by Eq. 3.3. The ratio of the rivet diameter to the sheet thickness must be less than 5.5 for the rivet to have an effective strength (Niu, 1999).

$$t \geq 1.5h \quad (3.3)$$

3.3 Material Selection

The selection of the materials to be used in the winglet structure was carried out following Ashby's methodology (Ashby, 2011). He has proposed the use of "material indices," which are ratios of material properties that are more significant for specific failure modes or types of loading. In his method, the best material for the particular application is the one with the lowest material index.

The structures in the winglet that take the majority of the load are the spar and the skin. The spar is required to resist bending and the skin must be able to resist buckling. Thus, the material for both must have high stiffness and high strength. The skin must be able to resist buckling and thus the material needs to have a high stiffness.

In aerospace structures weight should always be minimized, therefore the material must have high stiffness and strength while also minimizing weight. A ratio called material index can be obtained for specific design objectives (Ashby, 2011).

Ashby has shown that the material index for a beam loaded in bending is given by Eq. 3.4. For the same beam to have a high strength the material index is that of Eq. 3.5. The lowest material index provides the optimum material for the intended application.

$$M_1 = \frac{\rho}{E^{1/2}} \quad (3.4)$$

$$M_2 = \frac{\rho}{\sigma_y^{2/3}} \quad (3.5)$$

The upper and lower skin panels experience different loads in normal flight conditions; normally the upper panel is under compression while the lower panel experiences a tension load. For this reason the material allowable is different for each panel.

For the upper skin the material index of Eq. 3.5 is used because high compressive strength is sought, while for the lower skin panel the relevant index is that of Eq. 3.8.

$$M_1 = \frac{\rho}{E^{1/3}} \quad (3.6)$$

$$M_{2a} = \frac{\rho}{\sigma_c^{1/2}} \quad (3.7)$$

$$M_{2b} = \frac{\rho}{\sigma_t^{1/2}} \quad (3.8)$$

These material indices can be plotted to reduce the number of materials to be further analyzed. The first screening of the materials was done by narrowing the materials selection to only aluminum alloys, for which strength limits are presented in the Military Handbook for metallic materials in aerospace structures (1998). Advanced composite materials were not considered due to the lack of available strength data.

The material selection for the spar was made by plotting the material indices M_1 and M_2 against each other as shown in Fig. 3.3. The aluminum alloys analyzed were 2000, 6000, and 7000 series. The figure displays each material as an oval that envelopes the reported values of the mechanical property in question. The materials that were chosen to be further investigated are shaded in red. Materials used in other winglets are also presented in the figure, as reference; the material retrofitted in the GII is shown in blue and the one used in the KC-135 in yellow.

The closer the material is to the ideal curve the better it performs with respect to its closest axis. The best material, therefore, would appear at the lower left corner of the plot. Since no material is a clear winner, the materials closest to the black curve were further investigated.

The upper skin material selection was made by plotting M_1 against M_{2a} , as shown in Fig. 3.4. For the lower skin M_1 and M_{2b} were used (Fig. 3.5). It can be seen, for example, that 2024-T36 displays good qualities in tension, but performs poorly in compression.

The plots assisted in reducing the number of possible materials to be considered to only six. Since these alloys exhibit a good performance for all the conflicting objectives, it was possible to use a single material for all substructures of the winglet.

3.3.1 Selected Material

The material properties in Figs. 3.3, 3.4, and 3.5 correspond to a wide range of manufacturing processes. The specific properties of the six alloys were then retrieved

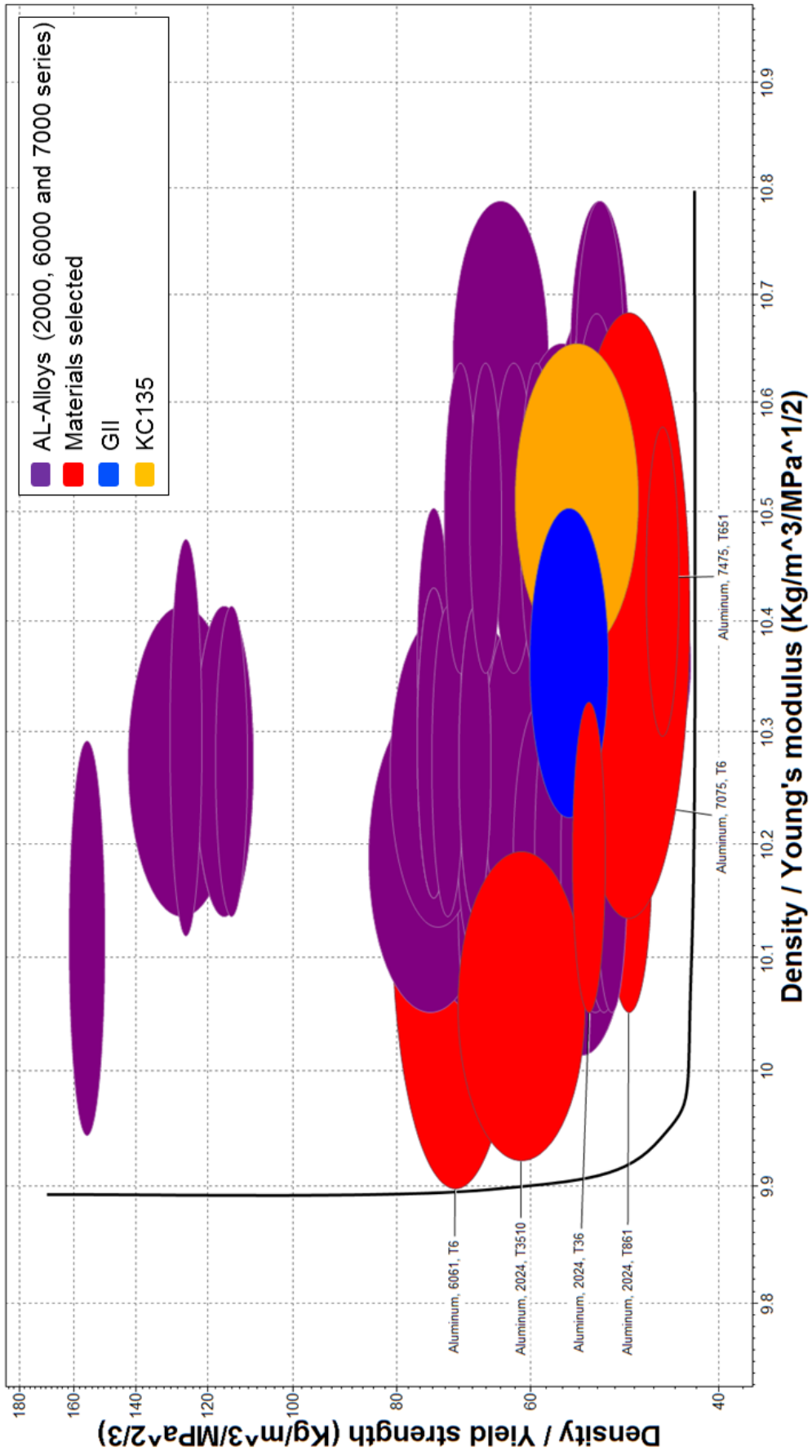


Figure 3.3: Ashby plot with conflictive objectives for the spar material.

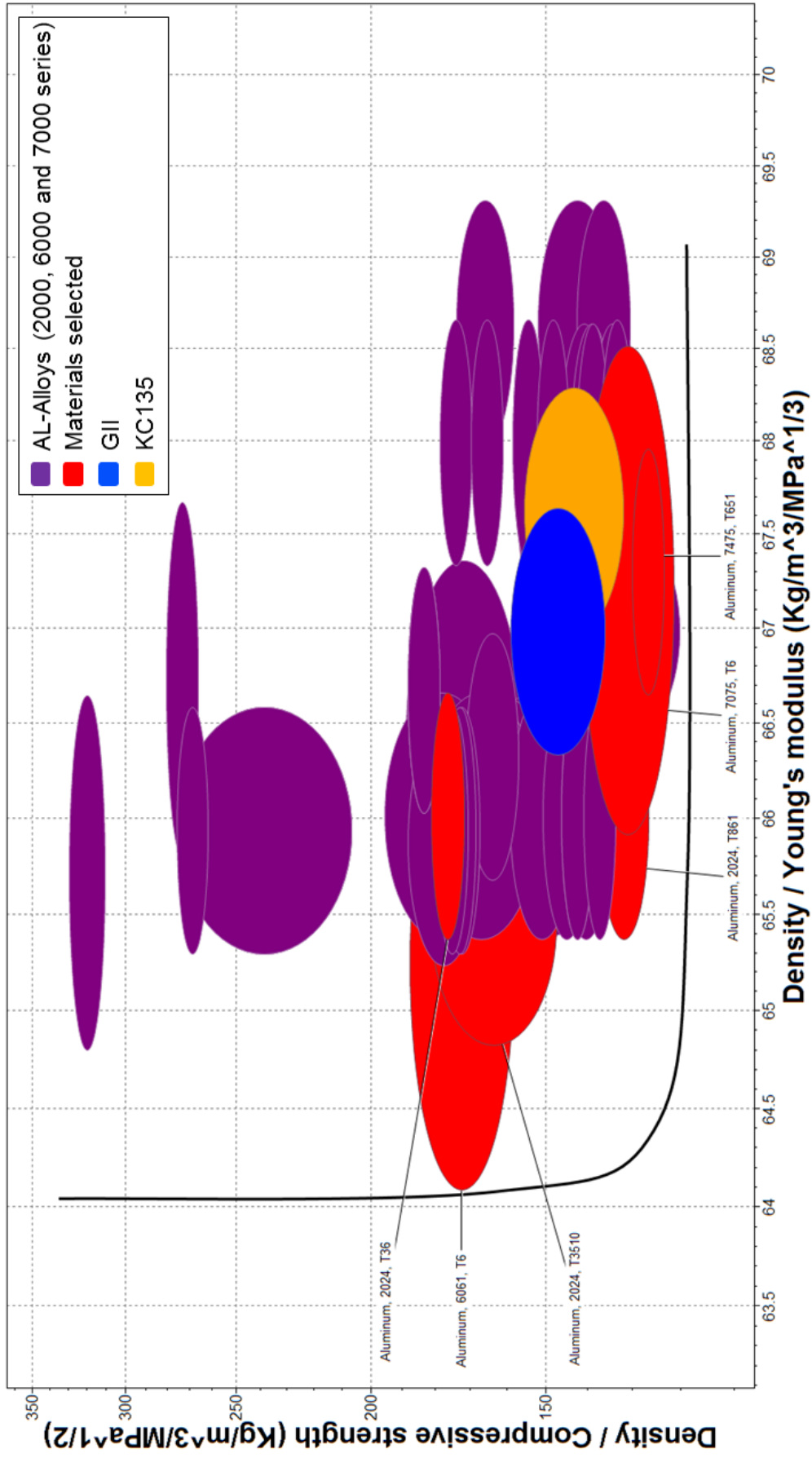


Figure 3.4: Ashby plot with conflicting objectives for the upper skin panel.

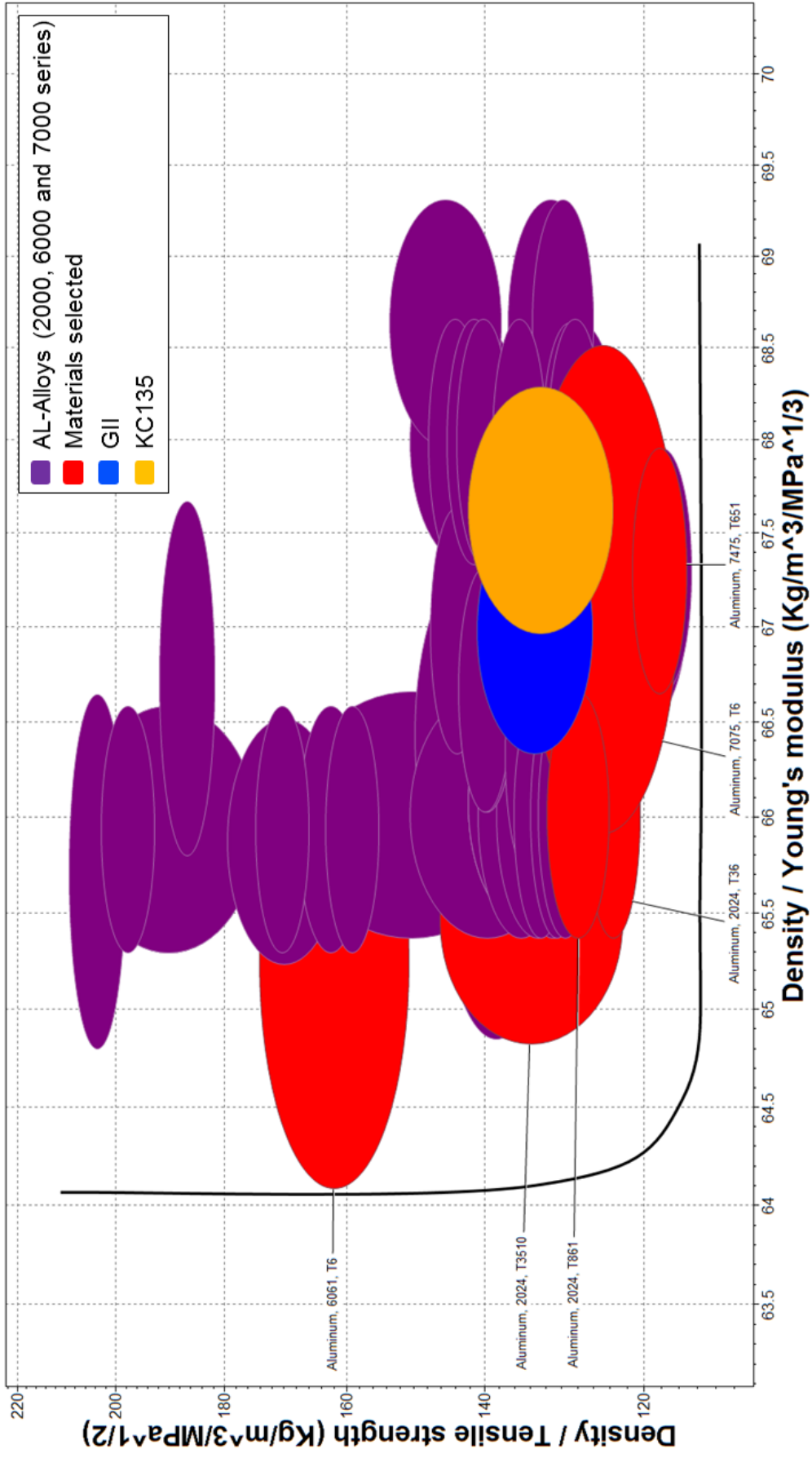


Figure 3.5: Ashby plot with conflicting objectives for the lower skin panel.

from the Military Handbook (1998), according to the respective manufacturing process and the approximate thickness of each structure. They are presented in Table 3.1, which shows that the Young's moduli are almost the same with the exception of Al 6061-T6, which is the lowest. However, this alloy also has the lowest density.

Table 3.1: Material selection summary.

	ρ (Kg/m ³)	E (GPa)	σ_t (MPa)	σ_c (MPa)
AL 2024-T3510	2,768	74	331	269
AL 2024-T36	2,768	72	365	310
AL 2024-T861	2,768	72	448	448
AL 6061-T6	2,713	70	248	241
AL 7075-T6	2,796	72	496	496
AL 7475-T651	2,796	73	407	407

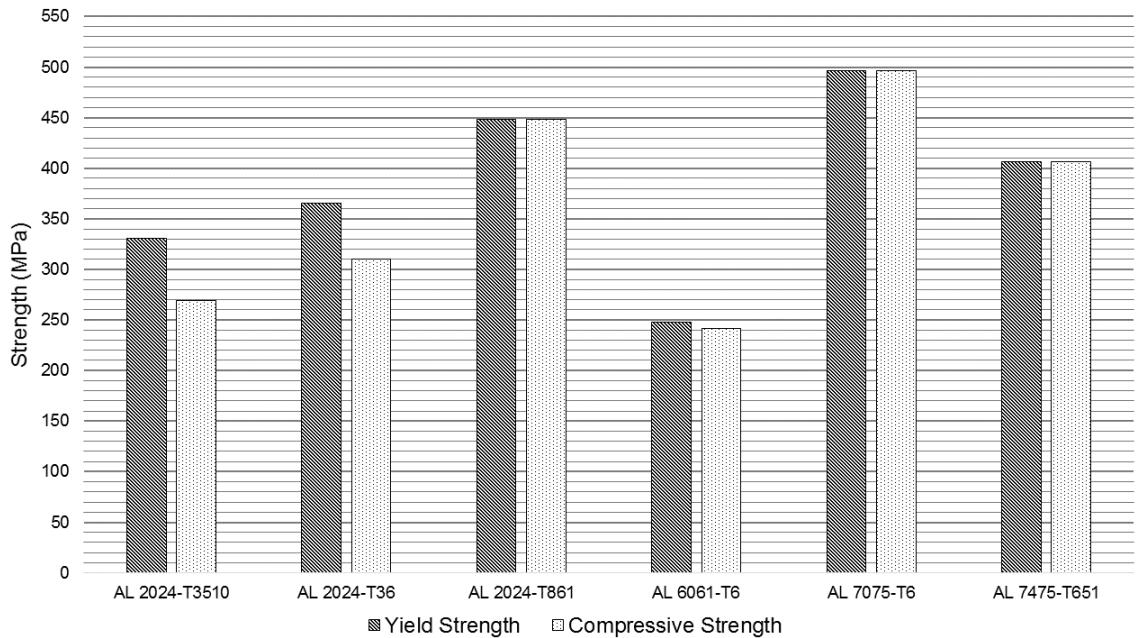


Figure 3.6: Comparison of strength between selected materials.

The bar graph in Fig. 3.6 compares the strength for the different alloys and heat treatments. Material AL 7075-T6 was selected for the winglet, because of its high strength in tension as well as compression.

3.3.2 Honeycomb Material

The dimensions of the winglet do not allow for the assembly of a full span spar. Instead, a full-depth honeycomb core is implemented in the design for the outer section.

The honeycomb sandwich is able to produce an efficient structure for resisting bending and buckling, because of the separation of the skins by the core. This separation increases the effective moment of inertia of the panel with a moderate increase in weight. Since the material selected for the winglet is aluminum, a typical honeycomb core material for aluminum skin panels, AL 5052, which is also used in the GII winglet (Mead et al., 1980), is used.

The mechanical properties of the core were taken from the HexWeb honeycomb sandwich design technology (2000) and are shown in Table 3.2. In order to obtain a fully orthotropic model to implement in the finite element model, the other mechanical properties were obtained from suggestions in the Hexcel description manual (Hexcel Composites, 2000). There is no relationship between the shear and elastic moduli, which means that the Poisson's ratio should be zero. A very small value was chosen for the Poisson's ratio in order to avoid a singularity in the finite element model. The compressive strength of the core is 4.2 MPa.

Table 3.2: Honeycomb material properties.

Material Property	Value (MPa)
E_1	≈ 0
E_2	≈ 0
E_3	517
G_{12}	≈ 0
G_{13}	310
G_{23}	152

3.4 Analysis Tools

The work presented here was performed using two computational tools: CES EduPack (2016) and ANSYS Workbench (2015). The former is an interactive database of material properties. It has the capability of plotting desired material properties to generate a visual representation, so that the users can assess the complex objective of selecting a material for their specific purpose.

ANSYS Workbench, was used due to its capability of coupling fluid dynamics with structural analysis. Aerodynamic loads can be generated using the Computational Fluid Dynamics (CFD) module Fluent, and then transferred to ANSYS Mechanical to be the applied loads of the finite element analysis. ANSYS Mechanical is capable of performing stress, thermal, modal, and fatigue simulations, and is also able to perform nonlinear stress simulations. It can model a variety of element behaviors and material models for different design problems.

3.5 Loads Development

Aerodynamic loads were estimated using a calibrated Fluent model (El Haddad, 2015). The calibration was carried out by matching the lift and drag curves with the wind tunnel tests performed by Dassault. The loading conditions presented in section 2.1 were used to obtain the pressure load on the winglet. For the roll flight condition, a calibrated vortex lattice model (El Haddad, 2015) was used. The pressure loads were then further analyzed to obtain the critical loading cases, as well as to examine the reactions at the connection. The sign convention for roll and sideslip angles is presented in Fig. 3.7.

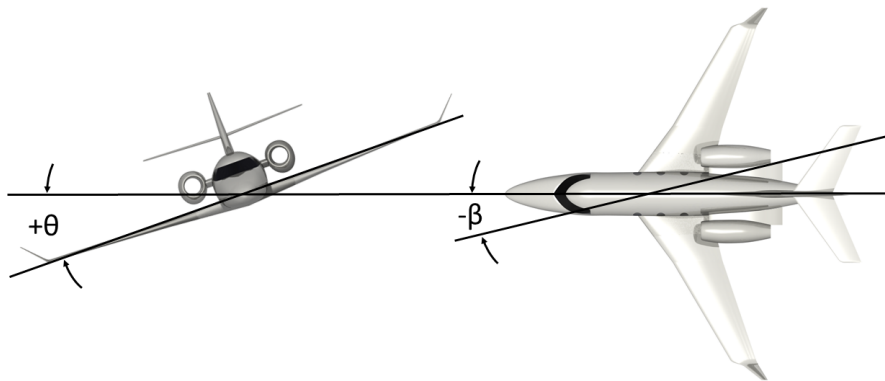


Figure 3.7: Sign convention used for roll and sideslip.

The winglet is connected to the wing at rib 16, so the pressures were analyzed from the rib to the tip in order to determine the reaction at the joint. Due to the change in angle of the structure, a coordinate, Ω , along the winglet midplane was used to plot the normal pressures (Fig. 3.9). The convention used for Ω and the

positive signs of shear and moment are presented in Fig. 3.8. It is important to note that the winglet bend occurs around 0.25 m from its root. That is the reason for the discontinuities in the pressure distribution curves.

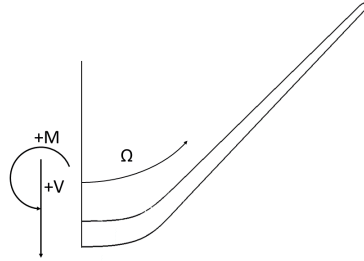


Figure 3.8: Reference axis used to plot load diagrams.

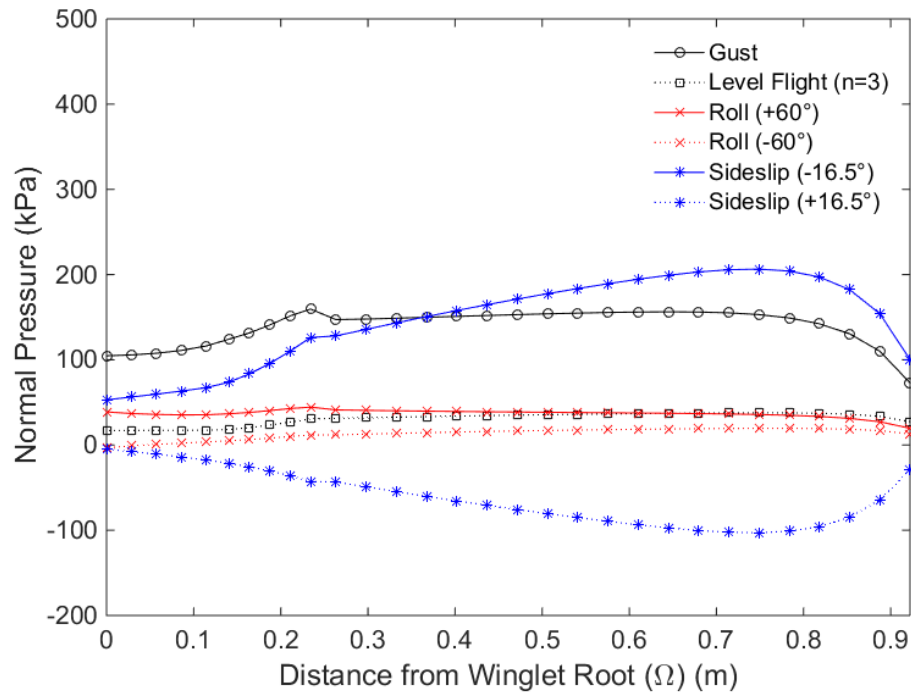


Figure 3.9: Normal pressure diagrams.

It can be seen that the highest lift is generated by the winglet in negative sideslip, because the freestream velocity is at a high angle of attack with respect to the port winglet. The lift generated during a positive sideslip condition, on the contrary, pushes the winglet outboard.

3.5.1 Shear and Moment Diagrams

The pressure loads were used to generate the shear and moment diagrams shown in Figs. 3.10 and 3.11, respectively.

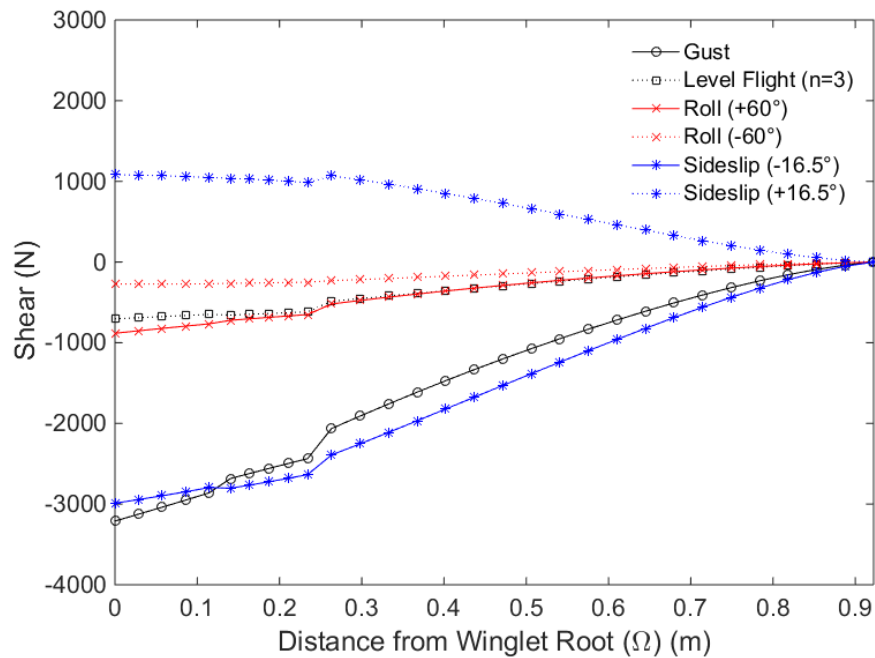


Figure 3.10: Shear diagram along Ω .

It can be concluded from the diagrams above that the most critical condition with respect to shear is the gust condition, followed by the negative sideslip. The positive

sideslip is also considered as critical due to the direction of the shear, which must be taken into account.

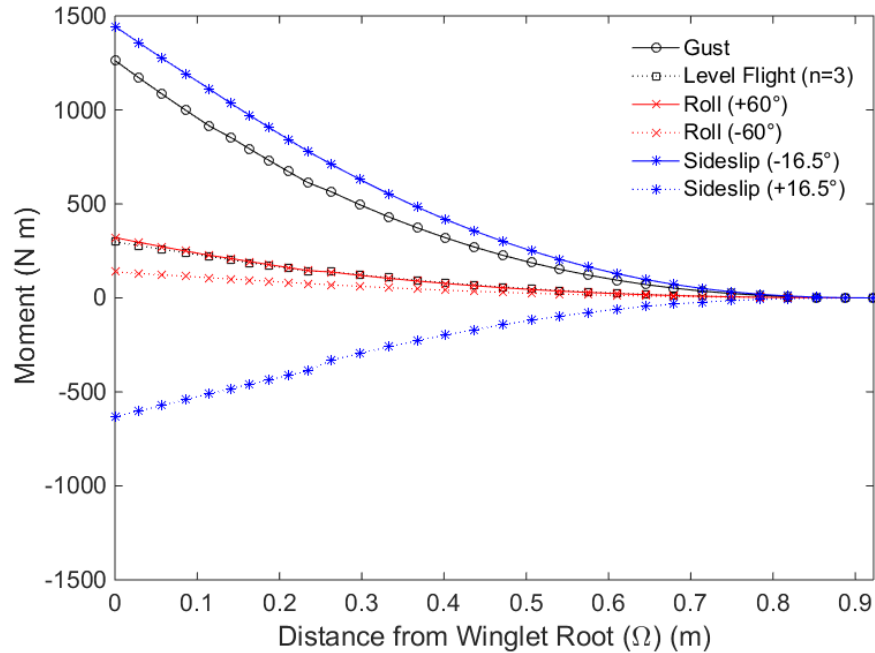


Figure 3.11: Moment diagram along Ω .

As expected, the negative sideslip flight condition has the highest bending moment, corresponding to the highest lift generated by the winglet. When encountering gust during flight a high moment is also created at the winglet root. The magnitude of the moment generated when positive sideslip is met is higher than at roll and level flight but in the opposite direction.

In summary, the three sizing loading cases chosen are the positive and negative sideslips, and the gust. The high loading factor on level flight does not generate higher shear or moments because at this condition the winglet does not generate much lift. Therefore they were considered non-sizing cases and not used.

3.5.2 Torsion Diagram

The proposed structural layout relies on one spar for both bending and torsion resistance. For this reason, a torsion diagram about the aerodynamic center (a.c.) was generated and presented in Fig. 3.12. The center of pressure moves away from the a.c. until reaching 0.15 m from the winglet root, where it starts to move closer to the a.c. as the distance from the winglet root increases. The change in center of pressure can be clearly seen in Fig. 3.12, as sudden changes in magnitude and slope. The gust load generates more lift in the section before the cant, so that the torsion is higher than during the sideslip condition. As expected, the positive sideslip condition creates torsion in the opposite direction to all other conditions. The most critical conditions for torsion are the same as those for shear and moment.

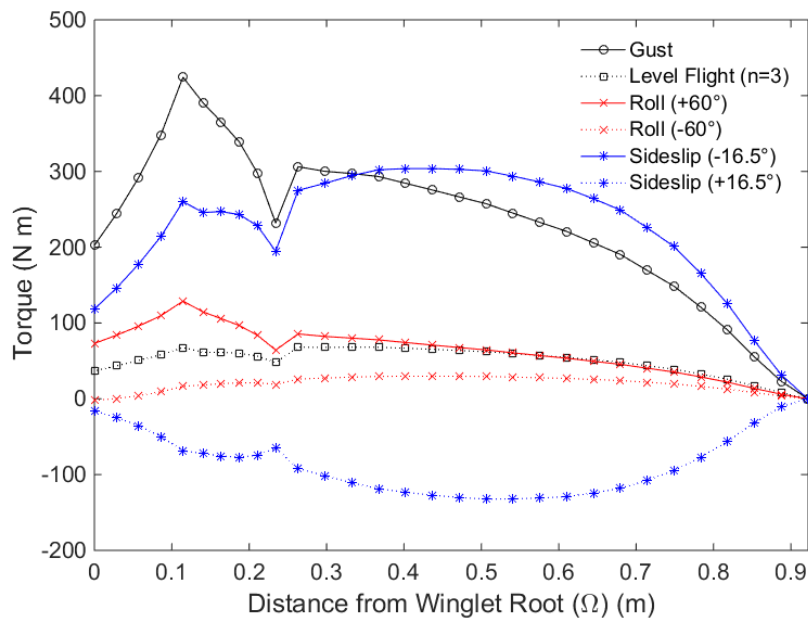


Figure 3.12: Torsion about the a.c.

3.6 Finite Element Analysis

A Finite Element Model of the structure was created to analyze the stresses and, using the failure modes and the material allowables, size the structural components.

3.6.1 Element Type

In this study, line elements were used to model beams, shell elements to model relatively thin structures, such as the skins, and solid elements for all other types of structure. Shell elements were preferred over solid elements because they provide accurate results at lower computational power and time.

Ribs, spars, and skins are relatively thin so shell elements were used to model these parts. The element designation name used for these parts is *Shell 281* (“ANSYS Mechanical User’s Guide”, 2015). This element’s diagram is shown in Fig. 3.13. It is an eight-node element with six degrees of freedom at each node. It is suitable for

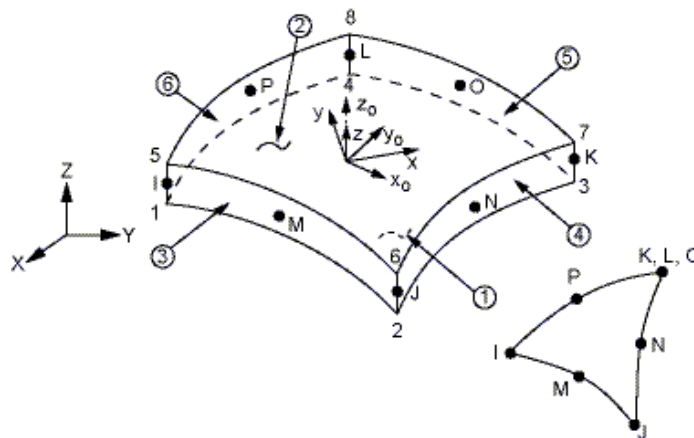


Figure 3.13: Representation of the element *Shell 281* (“ANSYS Mechanical User’s Guide”, 2015).

linear, large rotation and large strain nonlinear applications. One of the assumptions made with this element is that there is no slippage between element layers (“ANSYS Mechanical User’s Guide”, 2015).

The sandwich honeycomb core span is not sufficiently large compared to its height. Therefore, shell elements were not applicable and the core was modeled as a solid. The element designation name is *Solid 185* (“ANSYS Mechanical User’s Guide”, 2015), comprising eight nodes and three degrees of translational freedom at each node. For this element it is recommended to use multiple elements through the thickness to obtain more accurate transverse shear results. Orthotropic properties were applied to the solid body and their reference plane had to be rotated to match the axis of the honeycomb core cells. The element is shown in Fig. 3.14. Although different geometries are available for this element, the recommended shape is a prism (“ANSYS Mechanical User’s Guide”, 2015). However, due to the winglet geometry, it was not possible to have all the elements as prisms.

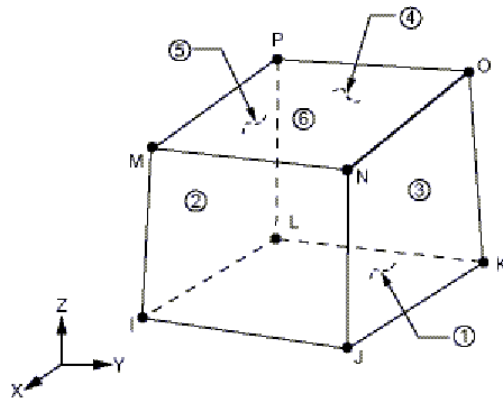


Figure 3.14: Representation of the element *Solid 185* (“ANSYS Mechanical User’s Guide”, 2015).

The fasteners were modeled with *Beam 188*, shown in Fig. 3.15. This is a linear element with six degrees of freedom at each node, and it includes the effect of transverse shear. This type of element can be used for linear, large rotation and large nonlinear strain applications. Its behavior is based on Timoshenko’s beam theory, which assumes that transverse shear strain is constant and that the cross-sections remain planar and undistorted following the deformation (“ANSYS Mechanical User’s Guide”, 2015).

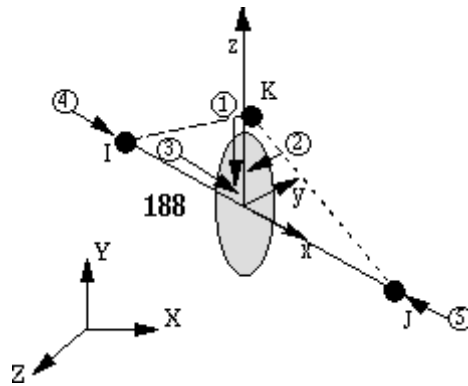


Figure 3.15: Representation of the element *Beam 188* (“ANSYS Mechanical User’s Guide”, 2015)

3.6.2 Load Application

The capabilities of ANSYS involve transferring aerodynamic loads from the CFD to the mechanical module for implementation in the structural analysis. In the winglet analysis, the pressures were applied to the upper and lower skin panels. Figure 3.16 shows a section view of the winglet with the pressures from the negative sideslip condition shown as vectors normal to the elements.

C: Limit Load (Negative Sideslip)
 Imported Pressure
 Unit: Pa

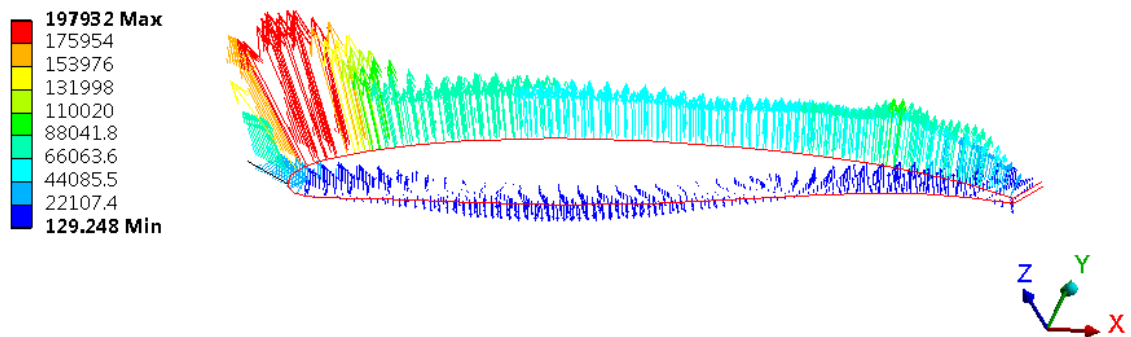


Figure 3.16: Application of pressure load on the winglet.

The fastened connections to the wing were analyzed using beam elements that connected the wing spars to the winglet spars and the wing to the winglet skins. The load from the nodes at the edges was transferred to a single node, which was then connected to the other structure as shown in Fig. 3.17.

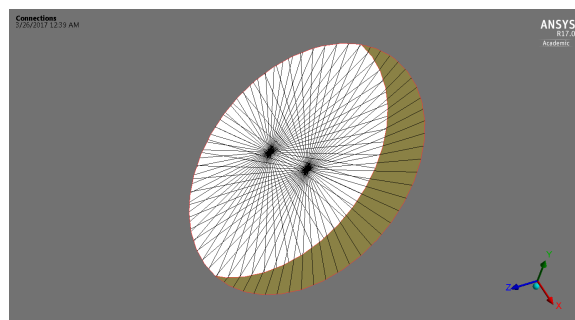


Figure 3.17: Spider web connection between spars.

3.6.3 Mesh Independence Study

A mesh independence study was conducted to ensure consistent results with the generated mesh. The three loading cases, as previously stated, are positive and

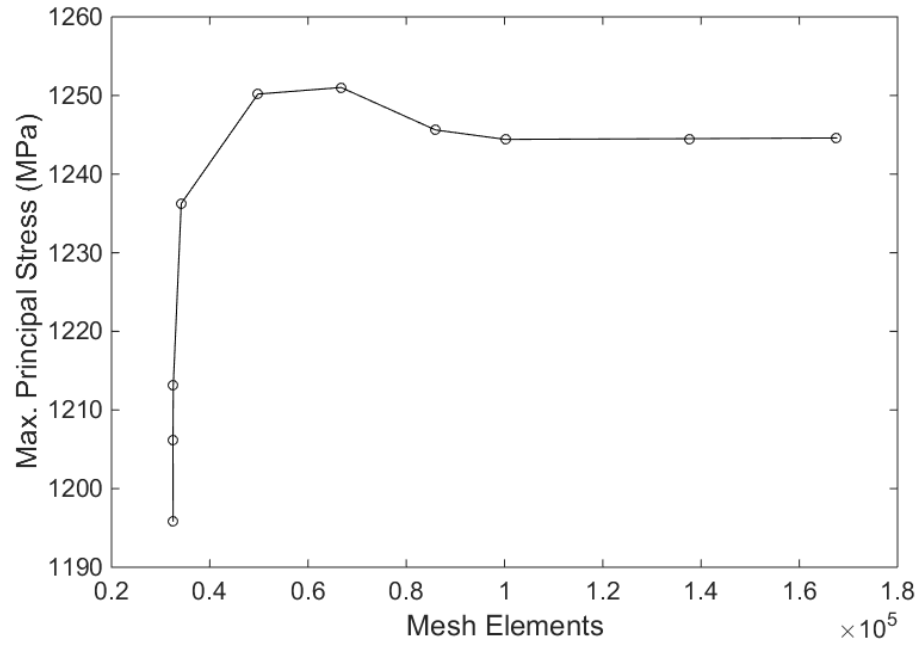


Figure 3.18: Mesh independence study with gust loading.

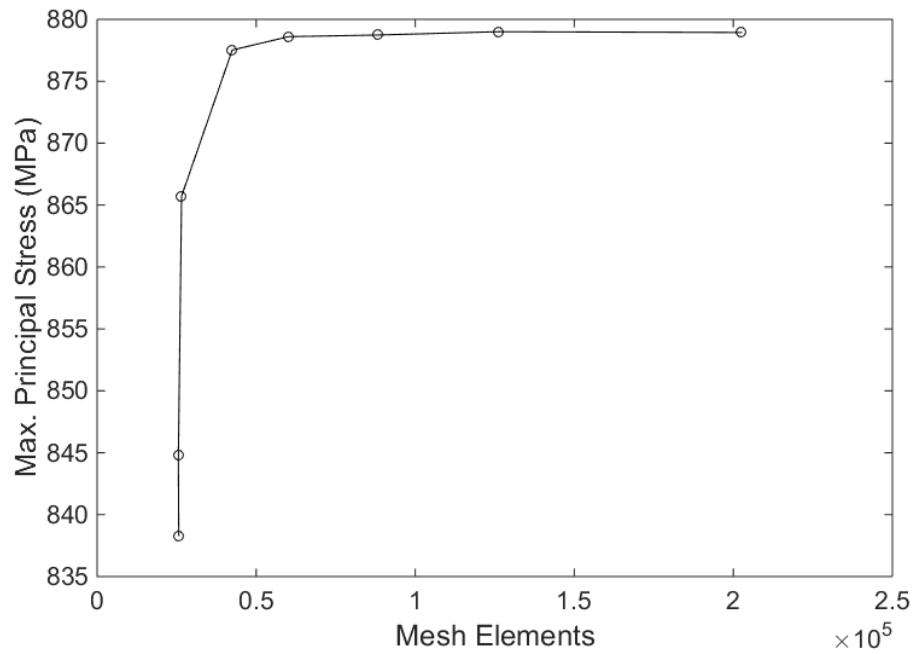


Figure 3.19: Mesh independence study with positive sideslip loading.

negative sideslip and gust. An initial thickness was given to the shell elements and the simulation was run by varying the size of the elements. In order to observe how the number of elements changed the results, the maximum principal stress across the entire structure was recorded and plotted. The mesh convergence plots for gust and, positive and negative sideslip are shown in Figs. 3.18, 3.19, and 3.20, respectively, and show that all of the loading cases stabilize at around 100,000 shell elements.

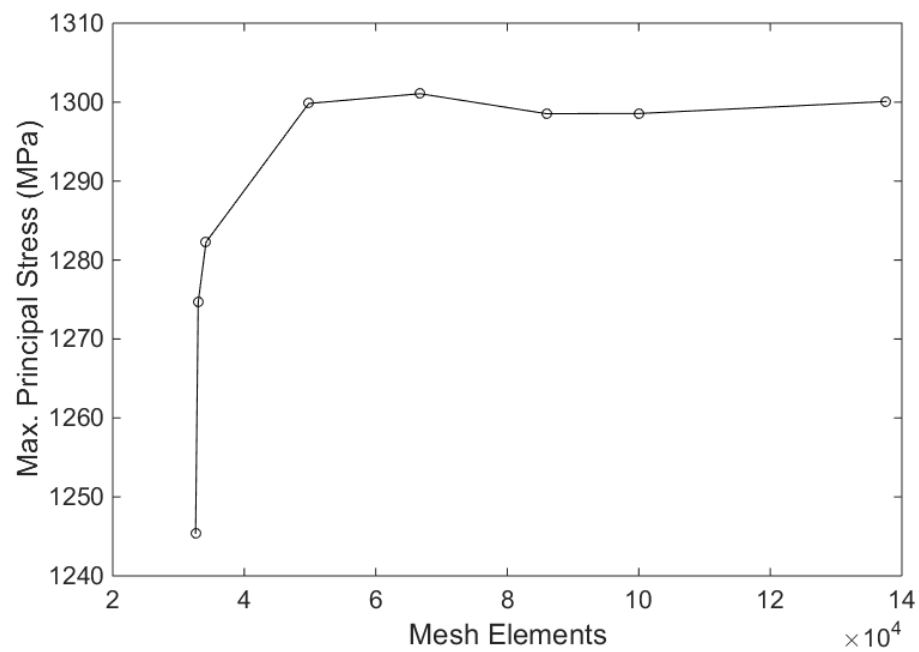


Figure 3.20: Mesh independence study with negative sideslip loading.

The final mesh used is comprised of 230,925 shell elements and 270,981 solid elements, with an average aspect ratio and an average corner angle of 1.82 and 103 deg, respectively.

3.7 Static Analysis

Failure is assumed to occur when the stress exceeds the material allowable. When considering the limit load, the stresses should remain below the elastic limit. In the present work, the principal stresses were compared to the material's yield stress. The von-Mises stress was also calculated and compared with the limit load when considering the yield stress.

The failure of the honeycomb core was estimated by looking into the different failure modes of a sandwich honeycomb structure. It has been established that there are five types of failure. The first failure occurs when the normal stress of the face is equal to the strength of the material. The next failure happens when the local instability stress of the compressed face is reached. The core fails when the principal stresses satisfy the yield criteria. The next failure is more difficult to analyze; it occurs when the bonding between the faces and the core fails. The analysis presented here only investigates the first three types of failures which dominate the failure map for sandwich structures shown in Fig. 3.21. The failure map is created by separating the variables from the equations that predict the failure load of the sandwich structure. The three variables are separated into those that describe the load, the material properties and the beam design. The map displays the boundaries where two mechanisms have the same failure load, which depend on the two design parameters used as axes. The box in Fig. 3.21 shows where common honeycomb structure designs are more prone to failure by face yield, face wrinkling, and core shear (Gibson and Ashby, 1999).

Primary failure of a honeycomb structure depends on the ratio t/l . At low values of this ratio, the faces tend to fail by wrinkling if the core density is low, and by yielding, if the core density is high. For high values of the ratio, the failure transitions from face to core by yielding in shear. Due to the fact that the honeycomb core is modeled as a solid, the shear stress cannot be used for analysis. Therefore, this model can only predict failures for a low t/l , which is the case for the winglet.

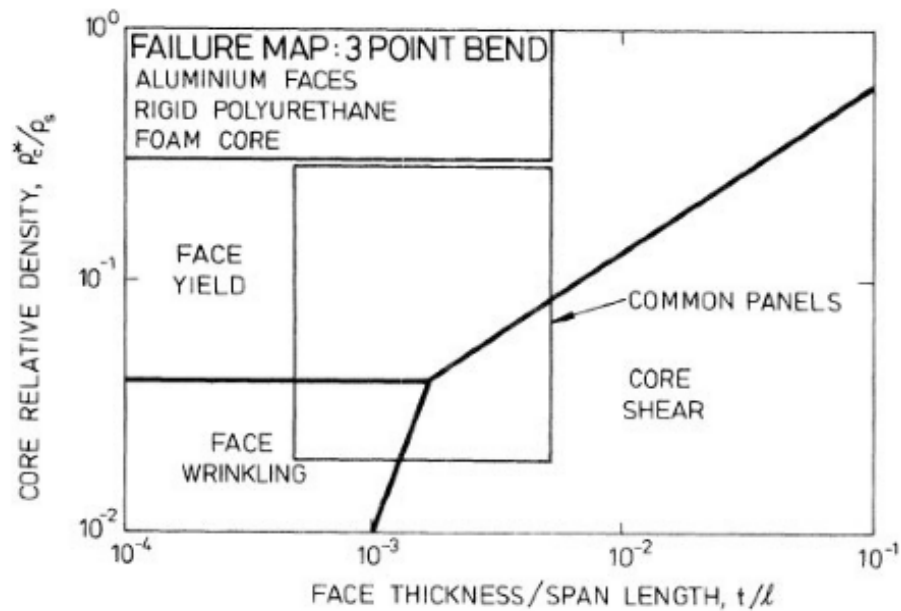


Figure 3.21: Failure map of a rectangular beam with honeycomb (Gibson and Ashby, 1999).

3.8 Buckling Analysis

The buckling analysis was carried out by implementing an eigenvalue buckling module in the program, which is able to predict the theoretical buckling strength of the ideal elastic structure. This type of analysis often yields quick but non-conservative results (“ANSYS Mechanical User’s Guide”, 2015).

4. Results and Discussion

The final dimensions of the winglet are shown in Table 4.1. The detail of the structure can be seen in the engineering drawings in the Appendix. The following section presents the stress results for each loading case with each loading type. The most critical load case was negative sideslip; during this load condition the winglet experiences the largest stresses. The maximum and principal stresses were compared with the ultimate strength of Al 7075-T6 for the ultimate load. When looking at the failure of the winglet at the limit load, the tensile and compressive yield strengths divided by the safety factor were used for comparison.

Table 4.1: Final design thicknesses.

	Thickness (mm)
Front spar web	2.0
Rear spar web	3.5
Rear spar lower cap	4.0
Rear spar upper cap	4.0
Rib 17	1.6
Rib 18	1.0
Slats cover	1.0
Aileron cover	1.0
Skin	5.2
Honeycomb skin panels	1.0

4.1 Ultimate Load

The summary of the stresses for negative and positive sideslip and gust are presented in Tables 4.2, 4.3 and 4.4, respectively. The margin of safety (MS) shown in these tables was calculated by using Eq. 4.1, where σ is the stress from the simulation being analyzed.

$$MS = \frac{\sigma_u}{\sigma} - 1 \quad (4.1)$$

Table 4.2: Stress at negative sideslip load.

	Maximum principal stress (MPa)	MS	Minimum principal stress (MPa)	MS
Front spar	163	2.3	-139	2.9
Rear spar	157	2.4	-238	1.3
Rear spar lower cap	305	0.8	-216	1.5
Rear spar upper cap	196	1.7	-274	1.0
Rib 17	228	1.4	-417	0.3
Rib 18	170	2.2	-176	2.1
Slats cover	87	5.2	-57	8.4
Aileron cover	209	1.6	-289	0.9
Honeycomb core	9.1	-	-3.7	0.1
Skin	417	0.3	-473	0.1

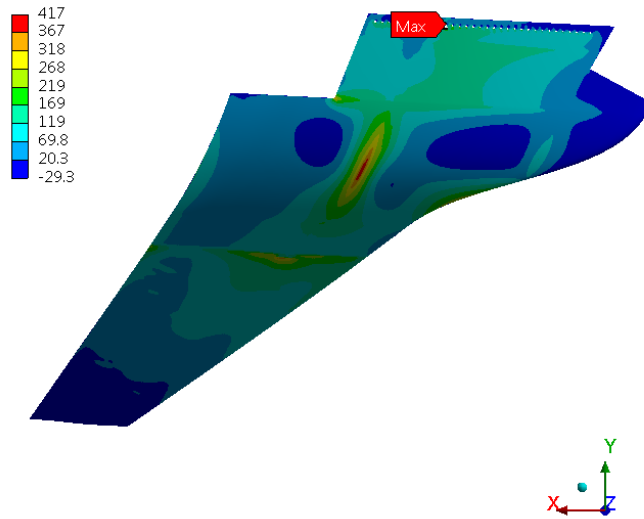
Table 4.3: Stress at positive sideslip load.

	Maximum principal stress (MPa)	MS	Minimum principal stress (MPa)	MS
Front spar	110	3.9	-121	3.4
Rear spar	153	2.5	-96	4.6
Rear spar lower cap	144	2.8	-192	1.8
Rear spar upper cap	176	2.1	-129	3.2
Rib 17	222	1.4	-120	3.5
Rib 18	74	6.3	-72	6.5
Slats cover	48	10.2	-72	6.5
Aileron cover	148	2.6	-114	3.7
Honeycomb core	4.2	-	-2.7	0.6
Skin	285	0.9	-263	1.0

Table 4.4: Stress at gust load.

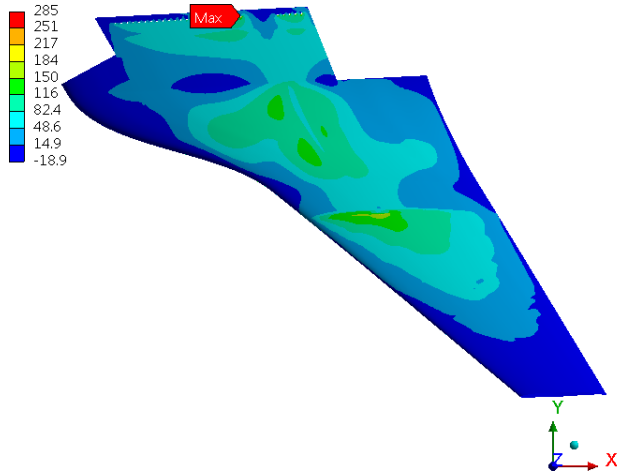
	Maximum principal stress (MPa)	MS	Minimum principal stress (MPa)	MS
Front spar	401	0.3	-387	0.4
Rear spar	323	0.7	-346	0.6
Rear spar lower cap	248	1.2	-177	2.1
Rear spar upper cap	156	2.4	-216	1.5
Rib 17	194	1.8	-357	0.5
Rib 18	132	3.1	-136	3.0
Slats cover	116	3.6	-90	5.0
Aileron cover	178	2.0	-251	1.1
Honeycomb core	7.3	-	-3.1	0.4
Skin	376	0.4	-427	0.3

B: Ultimate Load (Negative Sideslip)
 Lower Skin
 Type: Maximum Principal Stress - Top/Bottom
 Unit: MPa
 Time: 1
 Max: 417
 Min: -29.3



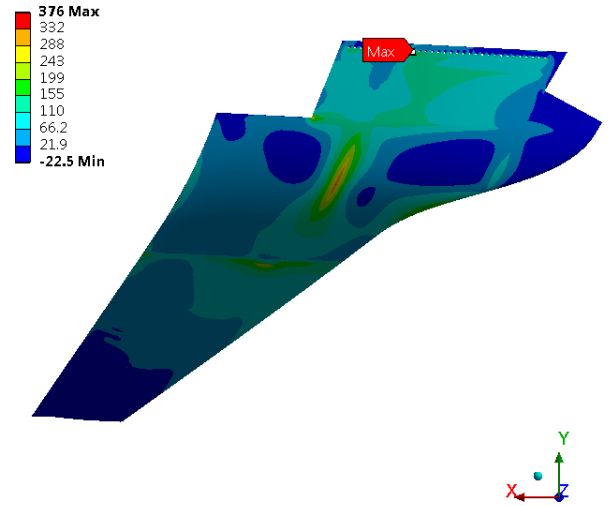
(a) Negative sideslip.

B: Ultimate Load (Positive Sideslip)
 Upper Skin
 Type: Maximum Principal Stress - Top/Bottom
 Unit: MPa
 Time: 1
 Max: 285
 Min: -18.9



(b) Positive sideslip.

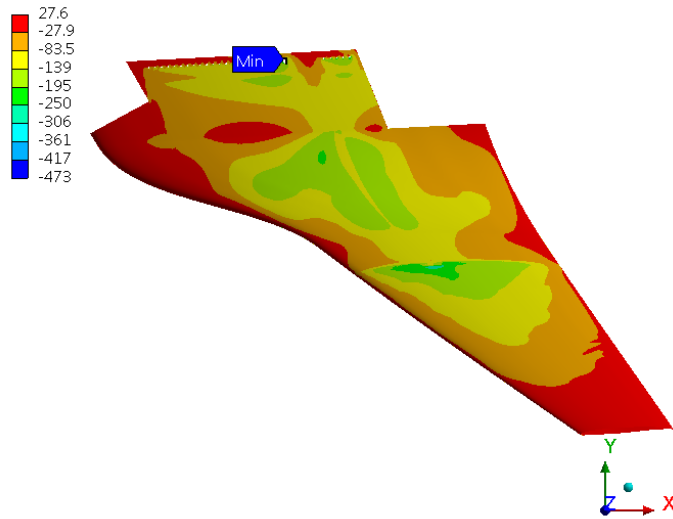
B: Ultimate Load (Gust)
 Lower Skin
 Type: Maximum Principal Stress - Top/Bottom
 Unit: MPa
 Time: 1



(c) Gust

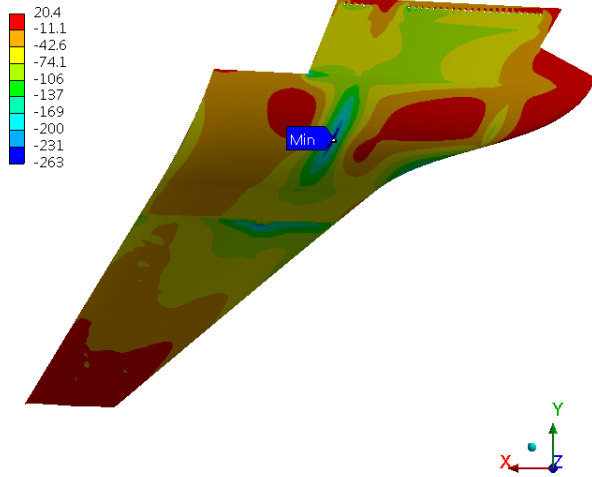
Figure 4.1: Maximum principal stress at ultimate load.

B: Ultimate Load (Negative Sideslip)
 Upper Skin
 Type: Minimum Principal Stress - Top/Bottom
 Unit: MPa
 Time: 1
 Max: 27.6
 Min: -473



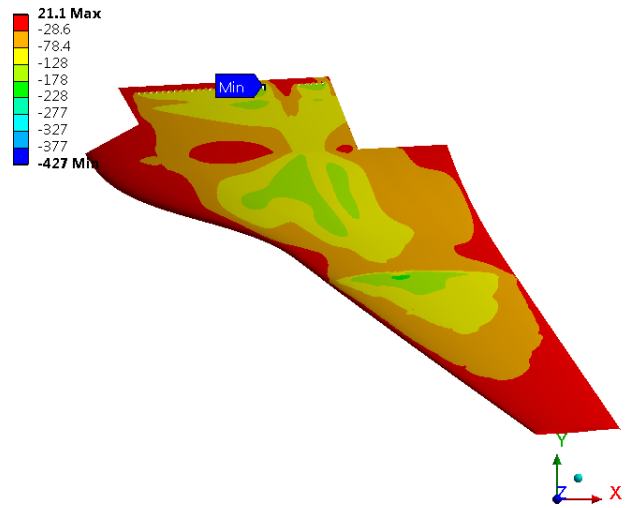
(a) Negative sideslip.

B: Ultimate Load (Positive Sideslip)
 Lower Skin
 Type: Minimum Principal Stress - Top/Bottom
 Unit: MPa
 Time: 1
 Max: 20.4
 Min: -263



(b) Positive sideslip.

B: Ultimate Load (Gust)
 Upper Skin
 Type: Minimum Principal Stress - Top/Bottom
 Unit: MPa
 Time: 1



(c) Gust

Figure 4.2: Minimum principal stress at ultimate load.

The maximum principal stress on the skin can be seen in Fig. 4.1. The upper skin panel is in tension when positive sideslip is experienced, and the lower skin panel is in tension for the negative sideslip.

The minimum principal stress on the skin can be seen in Fig. 4.2. The lower skin panel is in compression when positive sideslip is experienced, and the upper skin panel is in tension during gust and negative sideslip.

To prove that the fasteners do not shear off, the shear force was extracted from the simulation and the stress was calculated using the cross section of the respective fastener being investigated. The maximum shear stress of the bolt is $512MPa$ and the shear from the simulation is presented in Table 4.5.

Table 4.5: Shear stress on the bolts.

	Negative sideslip	Positive sideslip	Gust
Front spar bolt (MPa)	65	58	179
Rear spar bolt (MPa)	145	41	235

The strength of the bolts connecting the skin panels is $517MPa$, the bolt numbering scheme can be seen in Fig. 4.3 and the shear stress at the respective bolt and load condition are shown in Fig. 4.4.

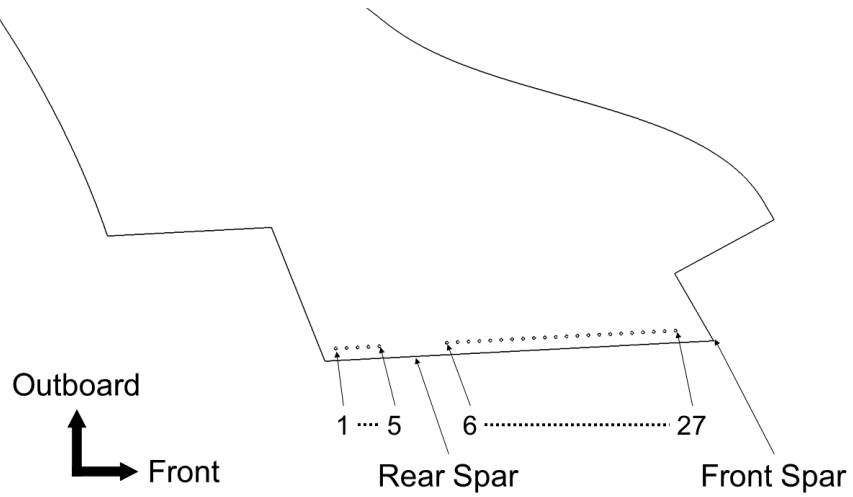


Figure 4.3: Bolt numbering.

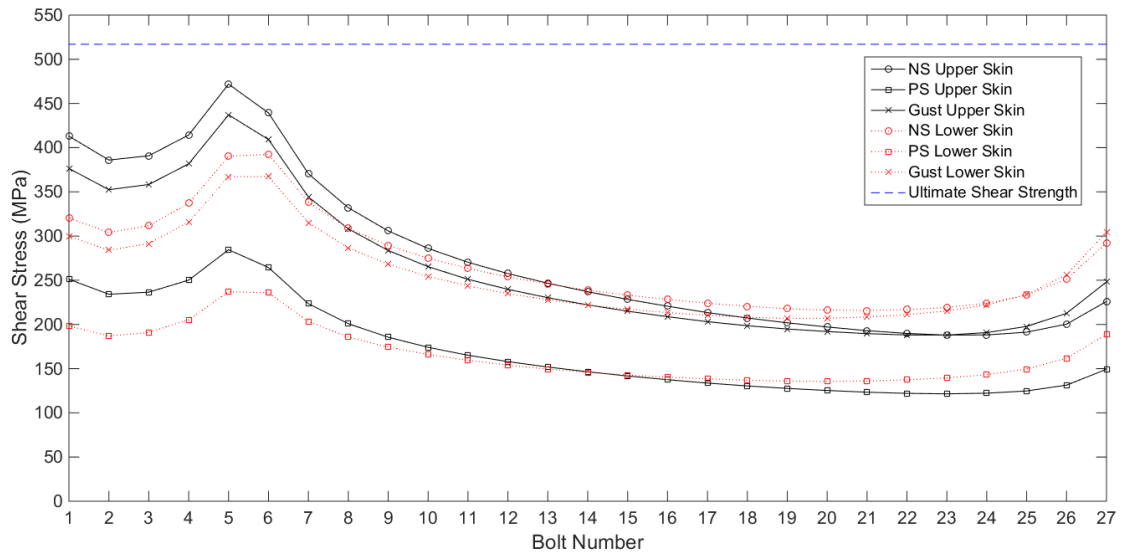


Figure 4.4: Shear stress per bolt.

The above graph show that the bolts are adequately sized for the shear experienced at the critical load cases.

4.2 Limit Load

The summary of the stresses at negative and positive sideslip and gust is shown in Tables 4.6, 4.7, and 4.8, respectively. The corresponding margin of safety was calculated by following Eq. 4.2. The tensile yield was used for the maximum and von Mises stresses, and compressive yield were used for the minimum stress.

$$MS = \frac{\sigma_y}{\sigma} - 1 \quad (4.2)$$

The maximum principal stress in the skin is shown in Fig. 4.5. The upper skin panel is in tension when positive sideslip is experienced and the lower skin panel is in the tension in the case of gust and negative sideslip. The minimum principal stress in the skin is shown in Fig. 4.6. The lower skin panel is in compression when positive sideslip is experienced, and the upper skin panel when gust and negative sideslip are

Table 4.6: Stress at negative sideslip load.

	Maximum principal stress (MPa)	MS	Minimum principal stress (MPa)	MS	Equiva- lent von-Mises (MPa)	MS
Front spar	109	3.4	-93	4.1	149	2.2
Rear spar	105	3.6	-159	2.0	176	1.8
Rear spar lower cap	203	1.4	-144	2.3	192	1.5
Rear spar upper cap	131	2.7	-182	1.6	198	1.4
Rib 17	152	2.2	-278	0.7	263	0.8
Rib 18	113	3.3	-117	3.1	104	3.6
Slats cover	58	7.3	-38	11.5	50	8.7
Aileron cover	139	2.5	-192	1.5	214	1.3
Honeycomb core	6.1	-	-2.4	-	6.9	-
Skin	278	0.7	-315	0.5	299	0.6

experienced. The equivalent von-Mises stress in the skin panels is shown in Fig. 4.7.

Table 4.7: Stress at positive sideslip load.

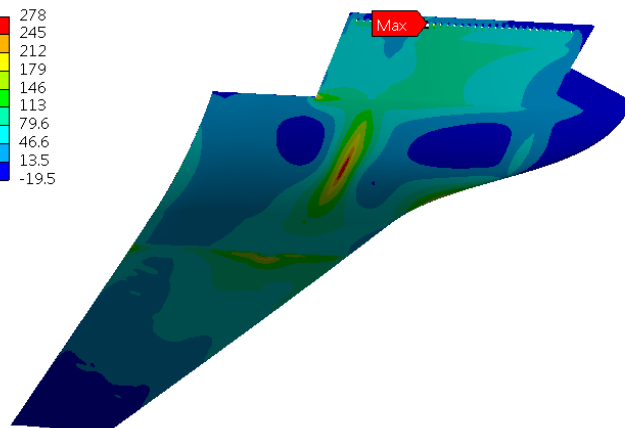
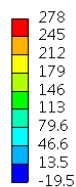
	Maximum principal stress (MPa)	MS	Minimum principal stress (MPa)	MS	Equivalent von-Mises (MPa)	MS
Front spar	73	5.6	-81	4.9	115	3.2
Rear spar	102	3.7	-64	6.4	108	3.5
Rear spar lower cap	96	4.1	-128	2.7	125	2.9
Rear spar upper cap	117	3.1	-86	4.6	129	2.7
Rib 17	148	2.3	-80	5.0	141	2.4
Rib 18	49	8.9	-48	8.9	47	9.3
Slats cover	32	14.1	-48	8.9	42	10.5
Aileron cover	99	3.9	-76	5.3	115	3.2
Honeycomb core	2.8	-	-4.0	-	4.4	-
Skin	190	1.5	-175	1.7	179	1.7

Table 4.8: Stress at gust load.

	Maximum principal stress (MPa)	MS	Minimum principal stress (MPa)	MS	Equivalent von-Mises (MPa)	MS
Front spar	267	0.8	-258	0.8	355	0.5
Rear spar	215	1.2	-231	1.1	242	1.0
Rear spar lower cap	165	1.9	-118	3.0	156	2.1
Rear spar upper cap	104	3.6	-144	2.3	156	2.1
Rib 17	129	2.7	-238	1.0	224	1.2
Rib 18	88	4.5	-91	4.2	81	5.0
Slats cover	78	5.2	-60	6.9	68	6.1
Aileron cover	119	3.1	-167	1.9	183	1.6
Honeycomb core	4.8	-	-2.1	-	5.5	-
Skin	251	0.9	-284	0.7	270	0.8

C: Limit Load (Negative Sideslip)

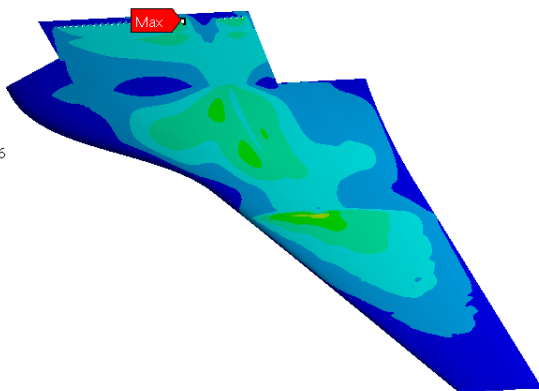
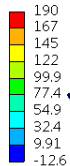
Lower Skin
 Type: Maximum Principal Stress - Top/Bottom
 Unit: MPa
 Time: 1
 Max: 278
 Min: -19.5



(a) Negative sideslip

C: Limit Load (Positive Sideslip)

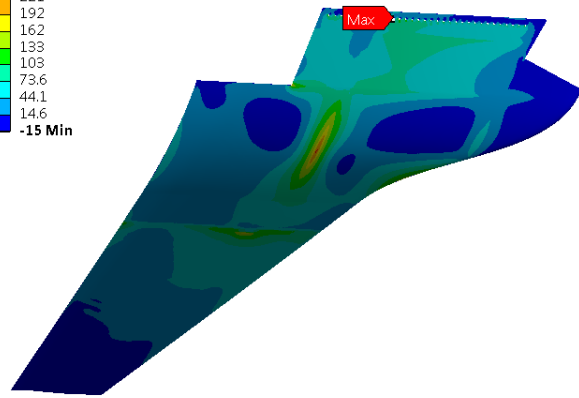
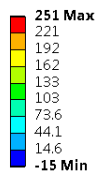
Upper Skin
 Type: Maximum Principal Stress - Top/Bottom
 Unit: MPa
 Time: 1
 Max: 190
 Min: -12.6



(b) Positive sideslip

C: Limit Load (Gust)

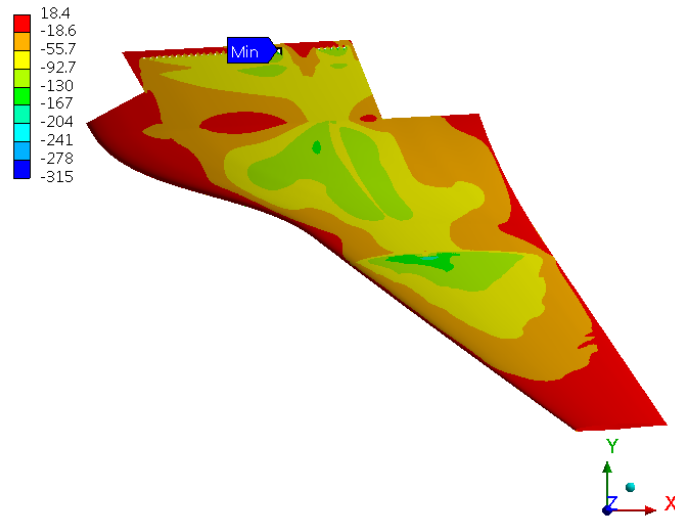
Lower Skin
 Type: Maximum Principal Stress - Top/Bottom
 Unit: MPa
 Time: 1



(c) Gust

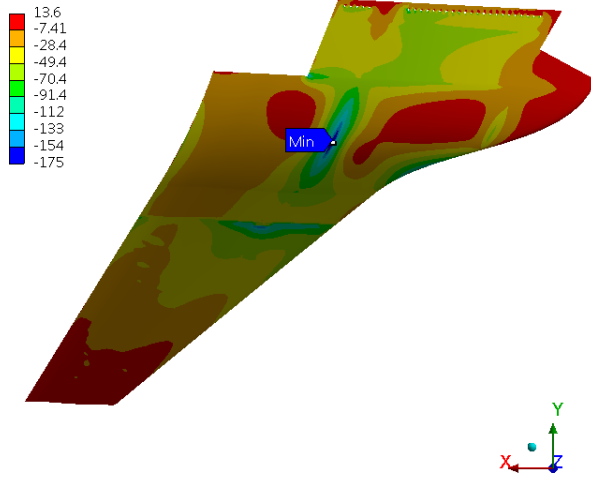
Figure 4.5: Maximum principal stress at limit load.

C: Limit Load (Negative Sideslip)
 Upper Skin
 Type: Minimum Principal Stress - Top/Bottom
 Unit: MPa
 Time: 1
 Max: 18.4
 Min: -315



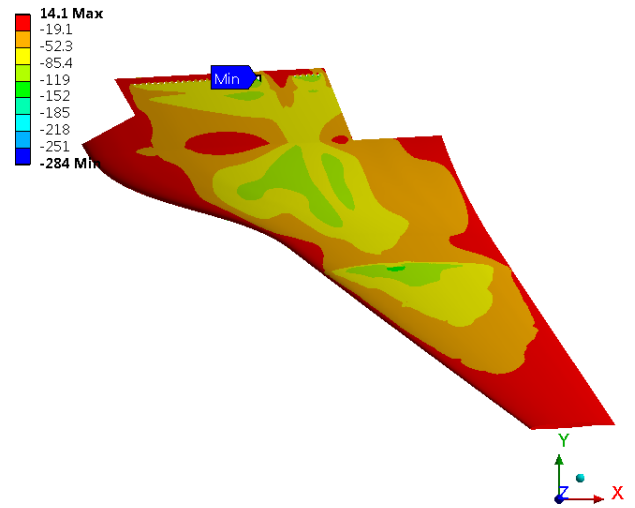
(a) Negative sideslip

C: Limit Load (Positive Sideslip)
 Lower Skin
 Type: Minimum Principal Stress - Top/Bottom
 Unit: MPa
 Time: 1
 Max: 13.6
 Min: -175



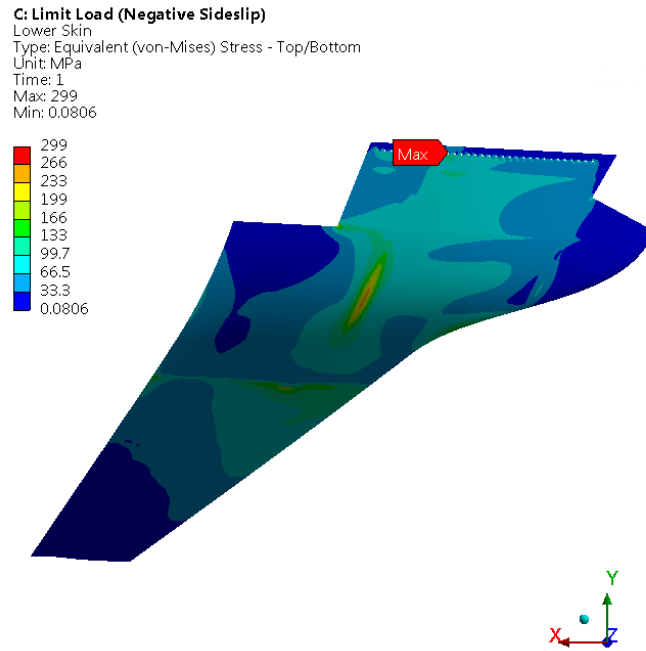
(b) Positive sideslip

C: Limit Load (Gust)
 Upper Skin
 Type: Minimum Principal Stress - Top/Bottom
 Unit: MPa
 Time: 1



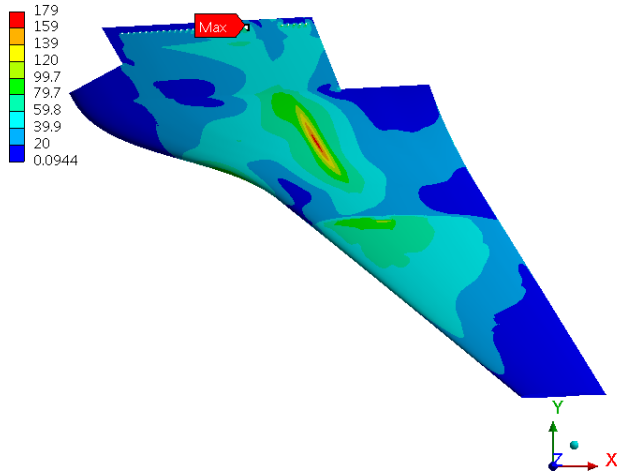
(c) Gust

Figure 4.6: Minimum principal stress at limit load.



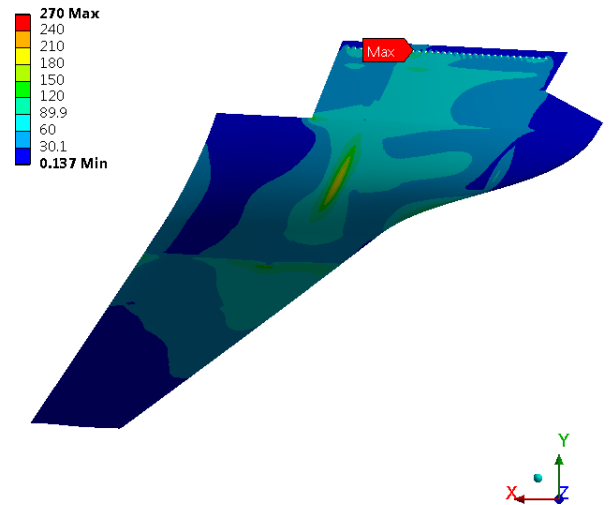
(a) Negative sideslip

C: Limit Load (Positive Sideslip)
 Upper Skin
 Type: Equivalent (von-Mises) Stress - Top/Bottom
 Unit: MPa
 Time: 1
 Max: 179
 Min: 0.0944



(b) Positive sideslip

C: Limit Load (Gust)
 Lower Skin
 Type: Equivalent (von-Mises) Stress - Top/Bottom
 Unit: MPa
 Time: 1



(c) Gust

Figure 4.7: Equivalent von-Mises stress at limit load.

4.3 Buckling

The results for the buckling modes for negative and positive sideslip and gust load are shown in Table 4.9. In order to prevent buckling the first mode must be greater than unity, and in the case where the load multiplier is less than zero the next positive multiplier should be higher than unity.

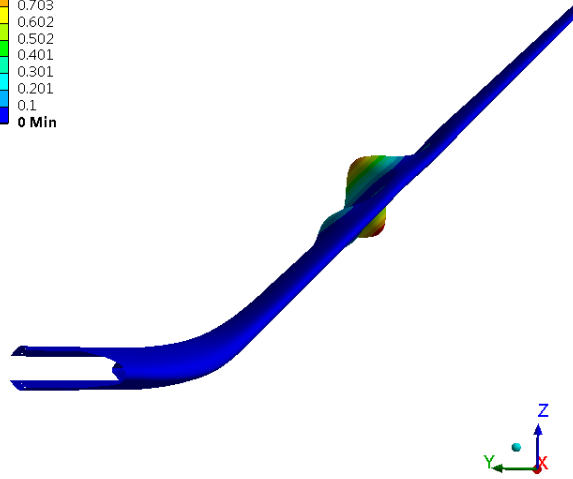
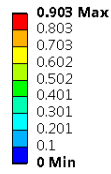
Table 4.9: Eigenvalue buckling with negative sideslip load.

Mode #	Negative sideslip	Positive sideslip	Gust
Mode 1	1.36	2.14	2.22
Mode 2	1.41	2.14	2.29
Mode 3	1.95	3.09	2.69

The graphic deformation representation of eigenvalue buckling is used to identify the part that is likely to fail under buckling. It also shows the mode shapes of the structure. The first mode of buckling for each loading case is shown in Fig. 4.8, where it can be seen that the skin face for the sandwich structure is the most likely component to fail under buckling.

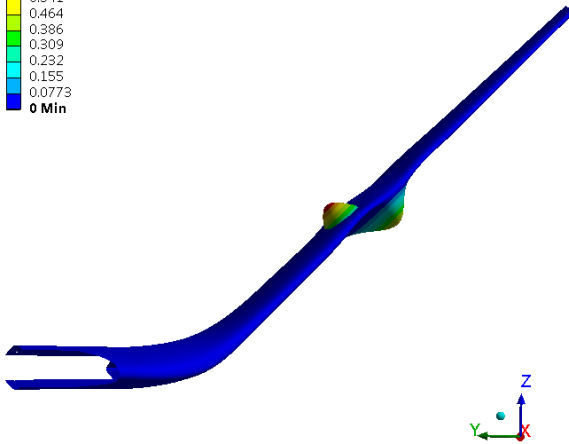
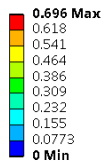
All of the load multipliers are higher than one so face wrinkling of the sandwich structure is avoided. The lower face is compressed during positive sideslip, so buckling is expected there. The upper face is compressed during negative sideslip and gust and, therefore, buckling is expected at this skin panel.

E: Eigenvalue Buckling (Negative Sideslip)
 Mode 1
 Type: Total Deformation
 Load Multiplier: 1.3625
 Unit: mm



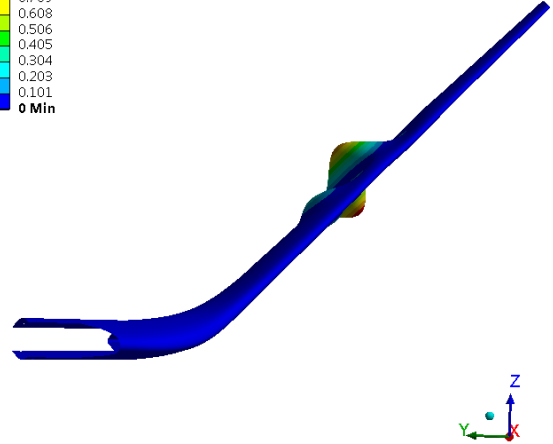
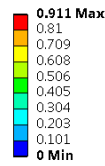
(a) Negative sideslip

E: Eigenvalue Buckling (Positive Sideslip)
 Mode 1
 Type: Total Deformation
 Load Multiplier: 2.1396
 Unit: mm



(b) Positive sideslip

E: Eigenvalue Buckling (Gust)
 Mode 1
 Type: Total Deformation
 Load Multiplier: 2.2223
 Unit: mm



(c) Gust

Figure 4.8: First mode buckling shapes.

5. Fabrication

This section describes the methods of fabrication for the different parts of the winglet. The winglet assembly and list of materials required are shown in Fig. 5.1.

The front and rear spars are forged into shape from an Al 7075 block, as specified in the engineering drawings, and are then the T6 heat treatment is applied. The bolt and rivet holes are drilled as specified.

The ribs are stamped into shape from a plate of clad Al 7075-T6. Rib 17 is machined from a plate to a final thickness of 1.6 mm, and the other ribs are 1 mm. The aileron and slat covers are stamped to shape. The holes for the rivets are drilled as specified.

The skin is composed of three sections for the upper and lower panels; the inspar, middle section, and core face skin panels comprise the skin of the winglet. The plates are stretched formed into the required shape.

The honeycomb core is milled to the contour of the winglet shape. The core is made of Al 5052 with a cell size of 3 mm and density of 72 kg/m^3 (HexWeb Honeycomb Sandwich Design Technology, 2000). The core has a higher density close to the connection with inboard section of the winglet, in order to allow proper fastening without degrading the mechanical properties of the sandwich. The tip of the sandwich is edge-filled to prevent moisture ingress. The connection to the rest of the winglet

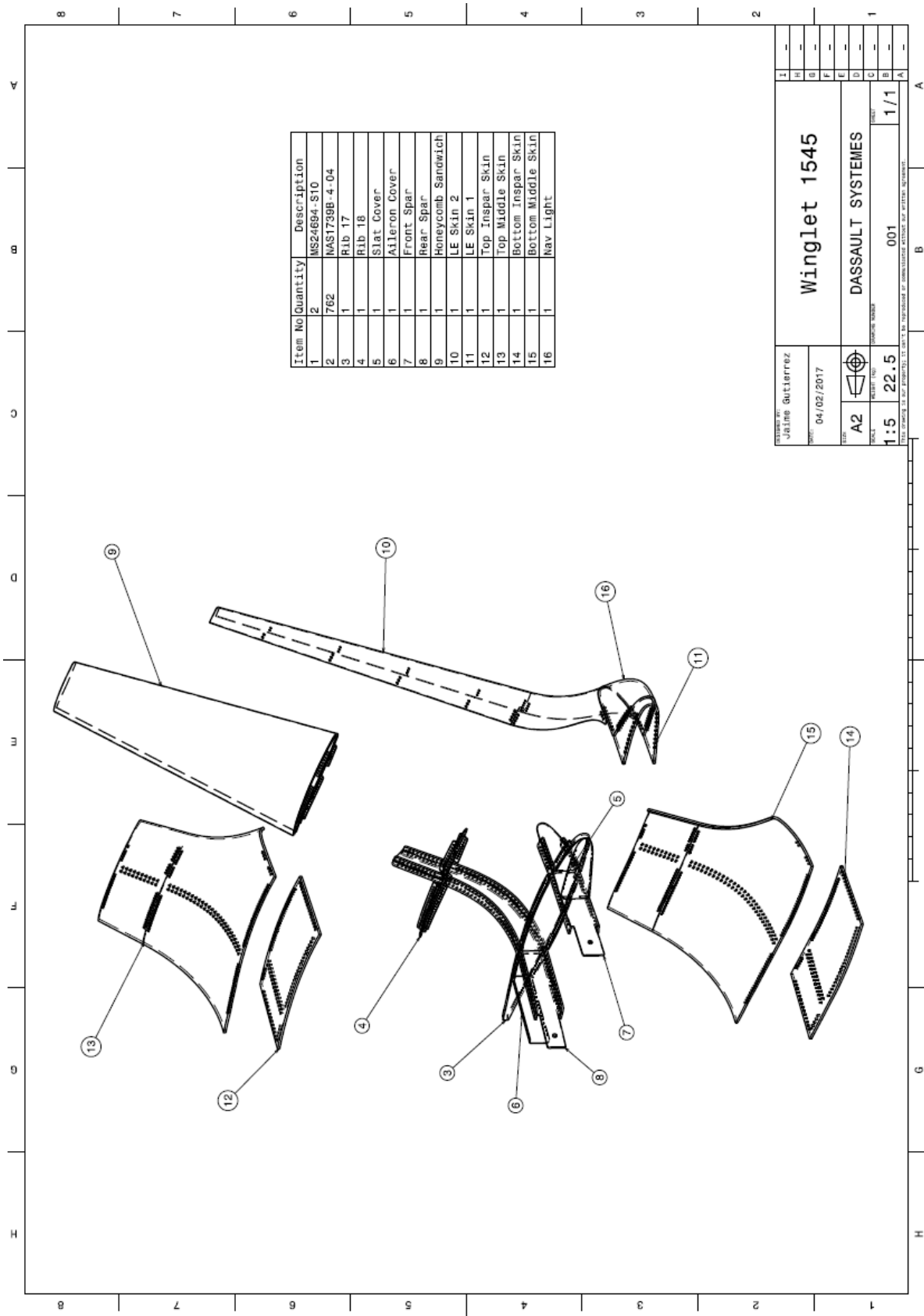


Figure 5.1: Bill of materials.

is made by a bonded edge closure section, which is then attached to the rear spar and middle skin section.

5.0.1 Fasteners

Two different types of fasteners are used to assemble the winglet. One type of bolt with two different sizes is used for the connection to the wing, and blind rivets are used for all other connections. Bolts are able to withstand higher shear stresses, and for this reason, they are used in highly loaded connections. They are also used in the connection to ease the replacement of the winglet.

Bolt MS24694 is presented in Fig. 5.2. It is countersunk to provide a flush contour with the skin. The specific dimensions and designation numbers are presented in Table 5.1.

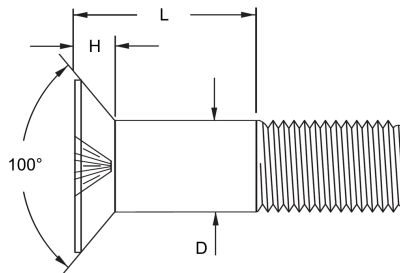


Figure 5.2: MS24694 bolt dimensions.

Table 5.1: Bolt dimensions.

	MS24694-S192	MS24694-S102
D	9.53 mm	6.35 mm
H	3.38 mm	2.69 mm
L	10.3 mm	10.3 mm

The rest of the fittings are carried out with blind rivets, as the size of the winglet restricts access for technicians to install solid rivets. The blind rivet used is NAS1739B-4-04, and is made out of Al 5056 and a steel alloy. Its dimensions are presented in Fig. 5.3 and Table. 5.2.

Table 5.2: NAS1739B-4-04 rivet dimensions.

NAS1739B-4-04	
D	3.18 mm
H	2.70 mm
L	10.3 mm
K	14.5 mm

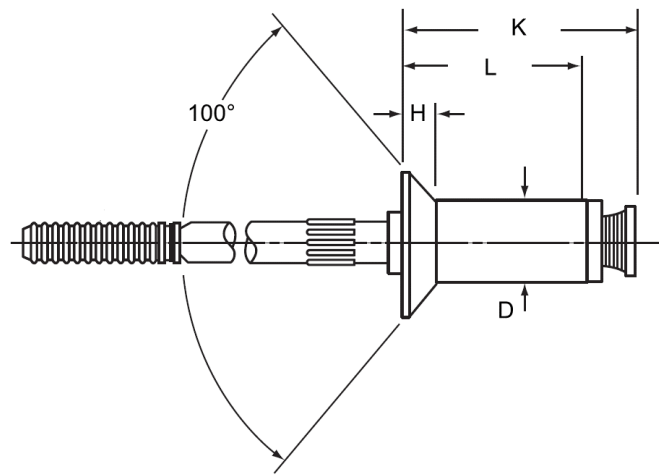


Figure 5.3: NAS1739B-4-04 rivet dimensions.

5.1 Winglet Assembly

The sandwich skins are pretreated with Redux primers and then bonded to the core by using Redux adhesive film (HEXCEL, 2017). The film is capable of with-

standing harsh environments such as high humidity and temperature. Ribs 17 and 18 are attached to the spars. The leading edge section of rib 17 is attached to the front spar as well as the slat cover. The other sections of the rib are then attached to the rear spar. Rib 18 is fastened to the rear spar. The rear and front spars are joined by the middle section of rib 17, and the anchor nuts are attached to them. The sandwich is then attached to the rear spar via the bonded edge closure. The inspar skin panel is fitted with anchor nuts. The skin panels are then riveted to the rest of the assembly.

5.2 Connection to the Wing

The installation of the winglet is performed by removing the wing tip from the wing. The wing skin panels are then reinforced, as specified by El Haddad (2015). The fastener holes are then drilled in the reinforced skin panels. The front and rear spar bolt connections are drilled. The flux valve access door allows the technicians to screw the bolt that connects the winglet's front spar to the wing box. The rear spar bolt is screwed in and the aileron cover is riveted to the skin, with rib 17 and rib 16 in the wing. Finally, the skin bolts are screwed in.

5.2.1 Corrosion Prevention

One of the most common causes of corrosion in aluminum alloys is the current flow between anodic and cathodic regions. The aluminum 7000 series is anodic with

respect to other aluminum alloys due to its zinc content. The 7075 alloy has a lower resistance to general corrosion than other 7000 alloys that do not contain copper. This series is also more resistant to general corrosion than the 2000 series. Although the 7000 series is more prone to stress-corrosion cracking (SCC), the addition of copper to 7075, which increases the strength of the alloy, also aids in resisting this type of corrosion (Davis, 1999).

Corrosion can be prevented by introducing a thin layer of pure aluminum or aluminum alloy. This layer must be selected so that it is anodic with respect to the core. The anodic layer lets the current flow through the electrolyte to the cathode and dissolve in the clad. The ion tends to preferentially dissolve and thus the cladding protects the core.

The clad layer for AL 7075 must be AL 7072, due to its higher anodic potential compared to pure aluminum. The thickness of the clad layer depends on the finished thickness of the part; one side of the sheet will be coated with a thickness of 1.2% of the specified thickness (Davis, 1999).

5.3 Weight Estimation

The weight of the winglet is estimated by using the tools in CATIA. The winglet is modeled and the material is applied to the different components, in order to obtain an estimation of the weight. The weight of the sandwich structure includes the weight of the skins, the core, and the adhesive film. The Redux adhesive film weighs 400 g/m² (HEXCEL, 2017). The results are shown in Table 5.3 and it can be noted that

the total estimated winglet weight is 22.5 kg, which is less than the weight estimated by El Haddad (2015).

Table 5.3: Weight summary.

	Weight (grams)
Front spar	435
Rear spar	1,007
Rib 17	422
Rib 18	92
Slats cover	46
Aileron cover	102
Honeycomb sandwich	4,590
Skin	15,506
Bolts and nuts	45
Blind rivets	211
Total	22,456

6. Conclusion and Future Work

The structural sizing of the winglet for the Falcon 10 was performed and presented in this study. The aerodynamic shape of the winglet and the calibrated CFD and vortex lattice models were taken from previous work and used to determine the aerodynamic loads for sizing. A layout design was then established to determine the dimensions, accessibility, and manufacturing capabilities enabled by the wing and winglet profile.

The selection of Al 7075-T6 as the material for the winglet was made by following the material selection process described by Ashby. The honeycomb core material, Al 5052, was chosen by investigating into the failure modes of the sandwich structures, as well as the materials employed in the past.

Critical load cases, consisting of negative and positive sideslip, and gust condition, were identified by looking into the generated shear, moment, and torsion diagrams. A finite element model was created and utilized to size the winglet with regards to ultimate and limit load conditions. Principal stresses were obtained to compare with the respective failure stress. Moreover, an Eigenvalue analysis was performed to assure the winglet does not fail under buckling. The shear force at the bolts was obtained and used to corroborate that the shear strength of the bolt is lower than its ultimate shear.

The fabrication and assembly process was described. The final weight of the winglet was estimated to be 22.5 kg which is less than the estimated weight by Nicolas. This weight reduction will improve the performance of the Falcon 10.

Further work should involve the accuracy evaluation of the FEA. The winglet should be manufactured and tested by implementing a whiffletree mechanism to apply the distributed load on the winglet. The effect of flutter on the structure must be investigated.

REFERENCES

- “A20X,” *Aeromet International LTD* [online database], URL: <http://www.aeromet.co.uk/a20x/index.html> [cited 15 March 2017].
- Anderson, N.H., *Aircraft Layout and Detail Design*, 2nd ed., McGraw-Hill Book Company, Novelty, OH, 1999.
- ANSYS Inc., *ANSYS Mechanical User’s Guide*, Ver. 17.0, Canonsburg, PA, 2015.
- ANSYS Workbench, Software Package, Ver. 17.0, ANSYS Inc., Canonsburg, PA, 2015.
- Ashby, M., *Materials Selection in Mechanical Design*, 4th ed., Elsevier Ltd., Oxford, 2011.
- CES 2016 EduPack, Software Package, Ver. 16.1, Granta Design Limited, Cambridge, 2016.
- Davis, J., *Corrosion of Aluminum and Aluminum Alloys*, 2nd ed., ASM International, 1999.
- El Haddad, N., “Aerodynamic and Structural Design of a Winglet for Enhanced Performance of a Business Jet”, Masters Dissertation, Aerospace Engineering Dept., Embry-Riddle Aeronautical University, Daytona Beach, FL, 2015.
- “Falcon 10 Airplane Flight Manual”, Avions Marcel Dassault Technical Report, 1972.
- “Falcon 10 sèrie, Calcul de la Voilure Première Partie”, Avions Marcel Dassault

Technical Report, 1972.

Faye, R., Laprete, R. and Winter, M., “Blended Winglets for Improved Airplane Performance”, *Boeing*, Jan. 2002.

Gibson L. and Ashby, M., *Cellular Solids: Structure and Properties*, 2th ed., Cambridge University Press, Cambridge, 1999.

Griffiths, B., “GKN Leads “STeM” Program to Successful Conclusion,” *Composites World* [online database], URL: <http://www.compositesworld.com/articles/gkn-leads-stem-program-to-successful-conclusion> [cited 15 March 2017].

HexWeb Honeycomb Sandwich Design Technology, Hexcel Composites, Stamford, CT, 2000.

Mead, L., Coppi, C., and Strakosch, J., “The Grumman Aerospace and Gulfstream American Gulfstream III Case Study in Aircraft Design”, *AIAA Professional Study Series*, 1980.

“Metallic Materials and Elements for Aerospace Vehicle Structures”, MIL-HDBK-5H, 1998.

Niu, C., *Airframe Stress Analysis and Sizing*, 2nd ed., Hong Kong Conmilit Press Ltd., Hong Kong, 1999.

“Redux 319L High Performance Modified Epoxy Film Adhesive,” *HEXCEL* [online database], URL: <https://www.silmid.com/adhesives/film-adhesives/redux-319-1-25sqm-freezer-storage-18c/> [cited 23 March 2017].

Torenbeek, E. and Wittenberg, H., *Flight Physics: Essentials of Aeronautical Disciplines and Technology*, 1st ed., Springer Netherlands, Dordrecht, NL, 2009.

Whitcomb, R., *A Design Approach and Selected Wind-Tunnel Results at High Subsonic Speeds for Wing-Tip Mounted Winglets*, NASA TND-8260, 1976.

A. Engineering Drawings

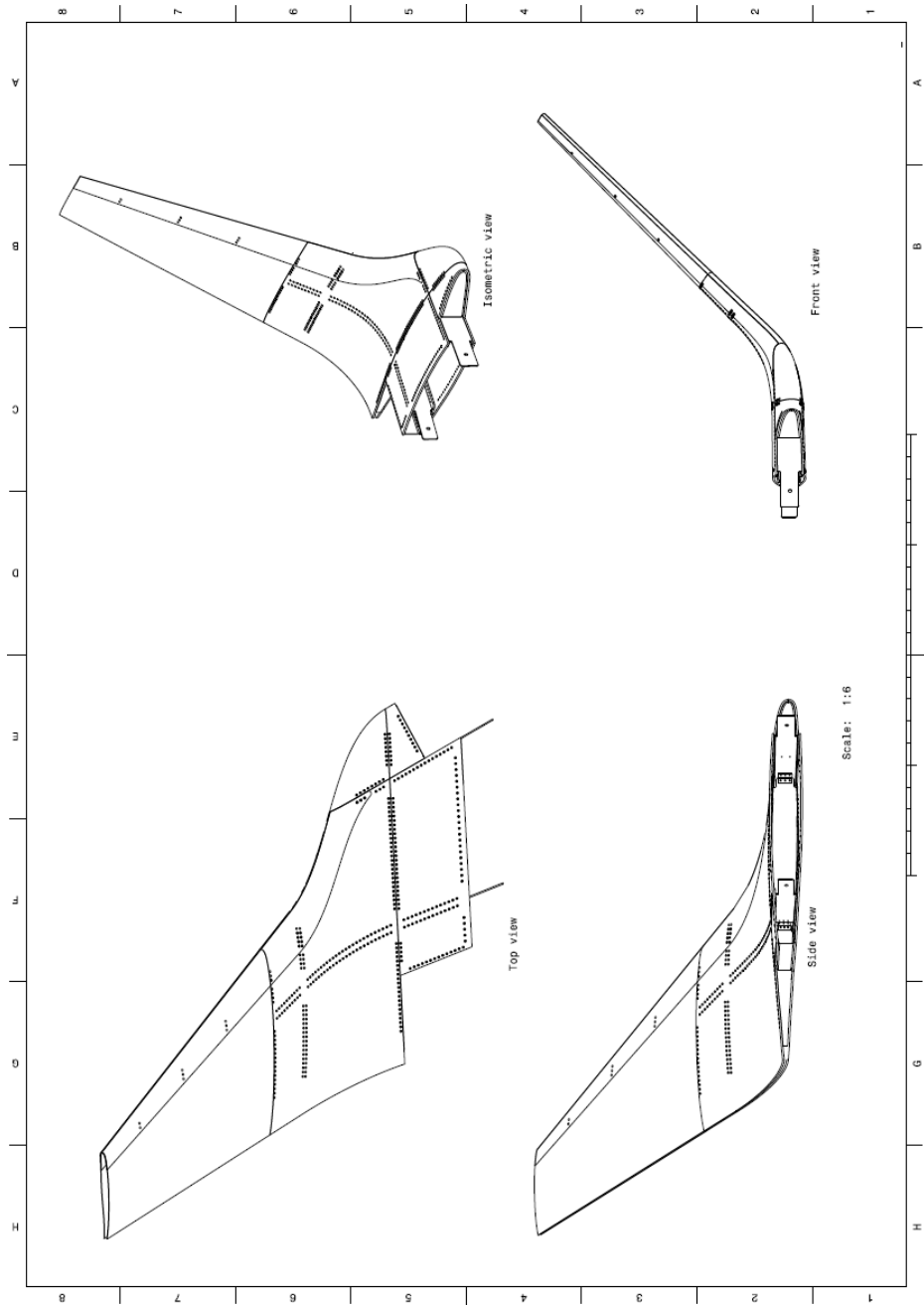


Figure A.1: 3 view drawing

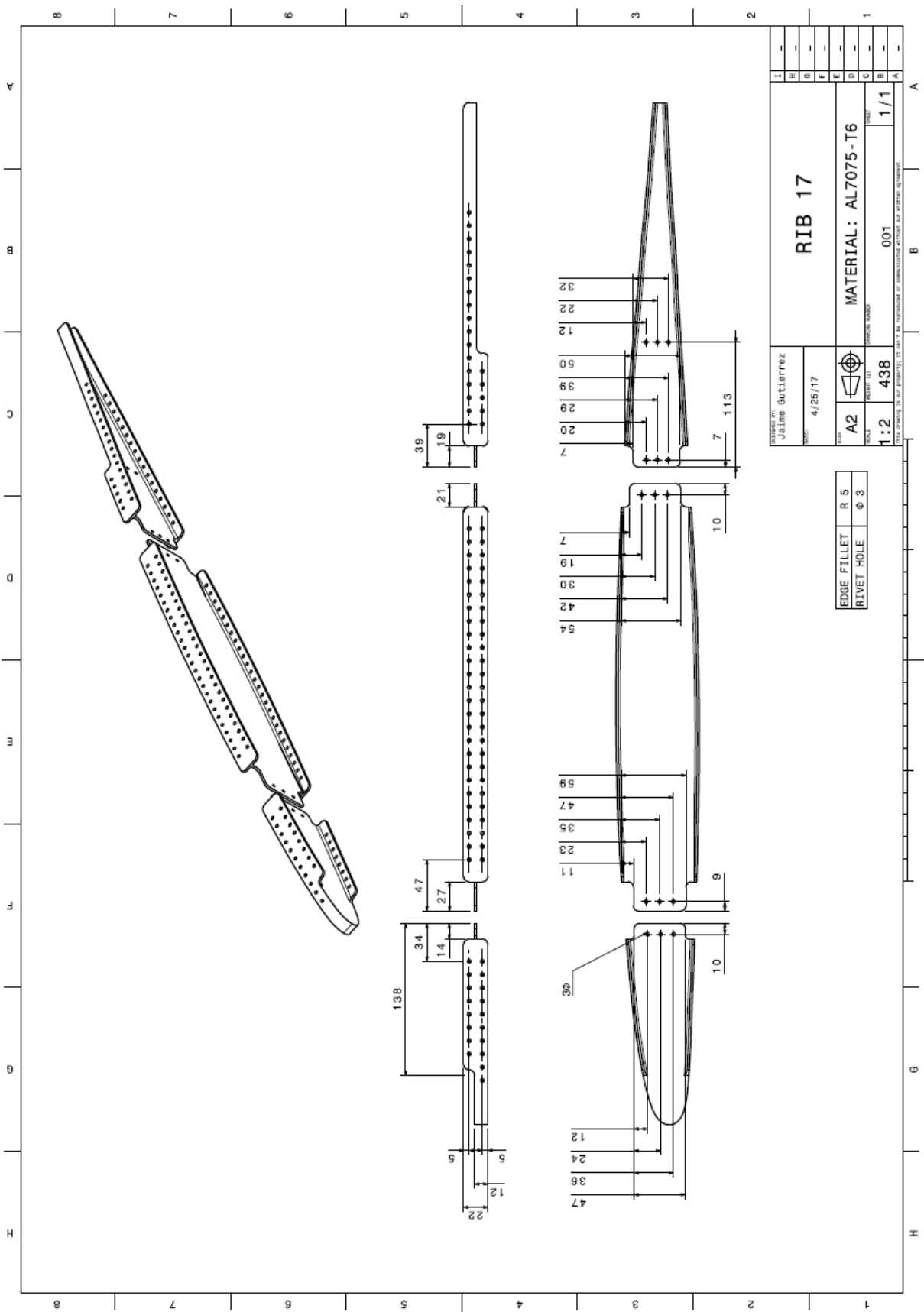


Figure A.2: Rib 17

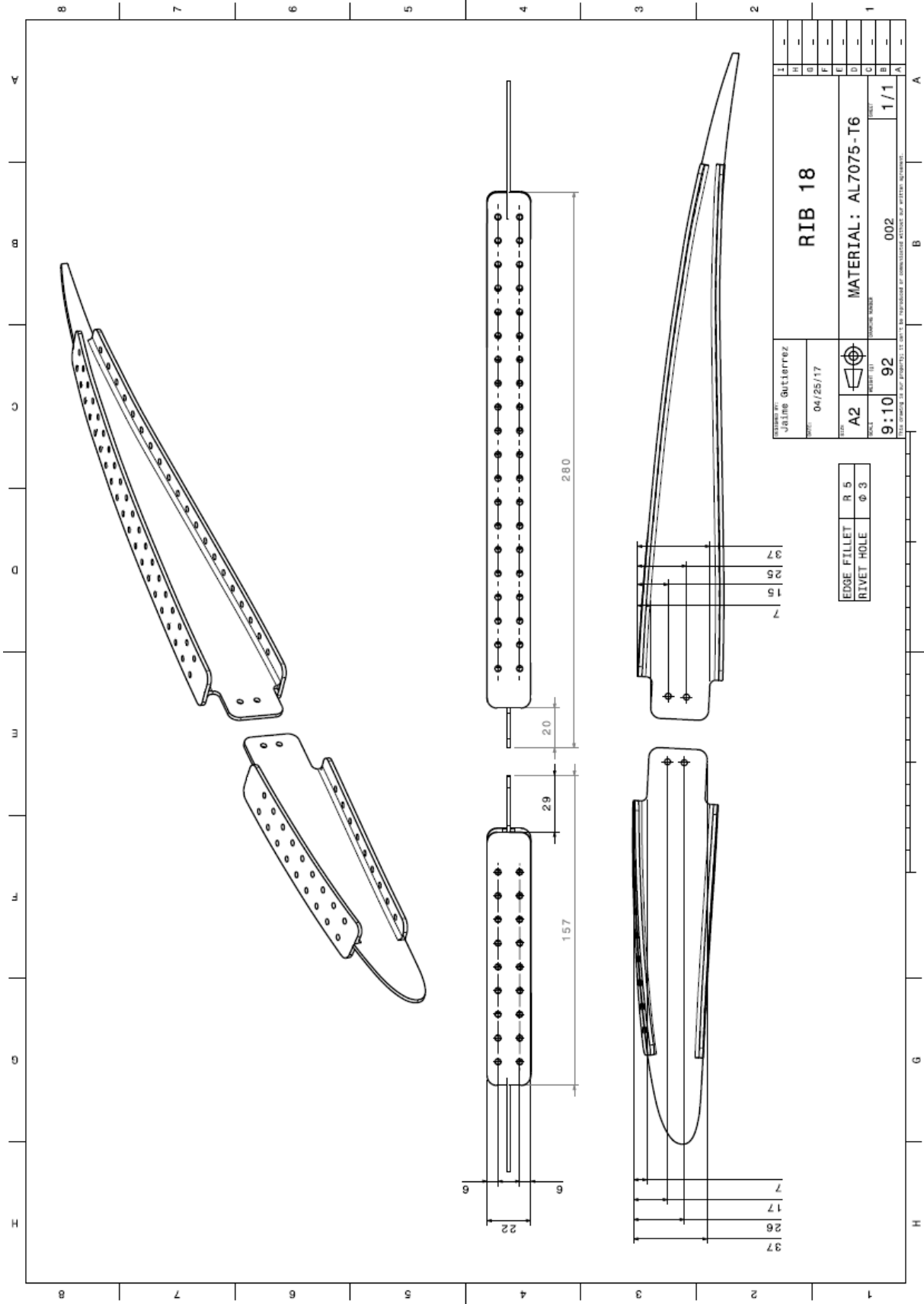


Figure A.3: Rib 18

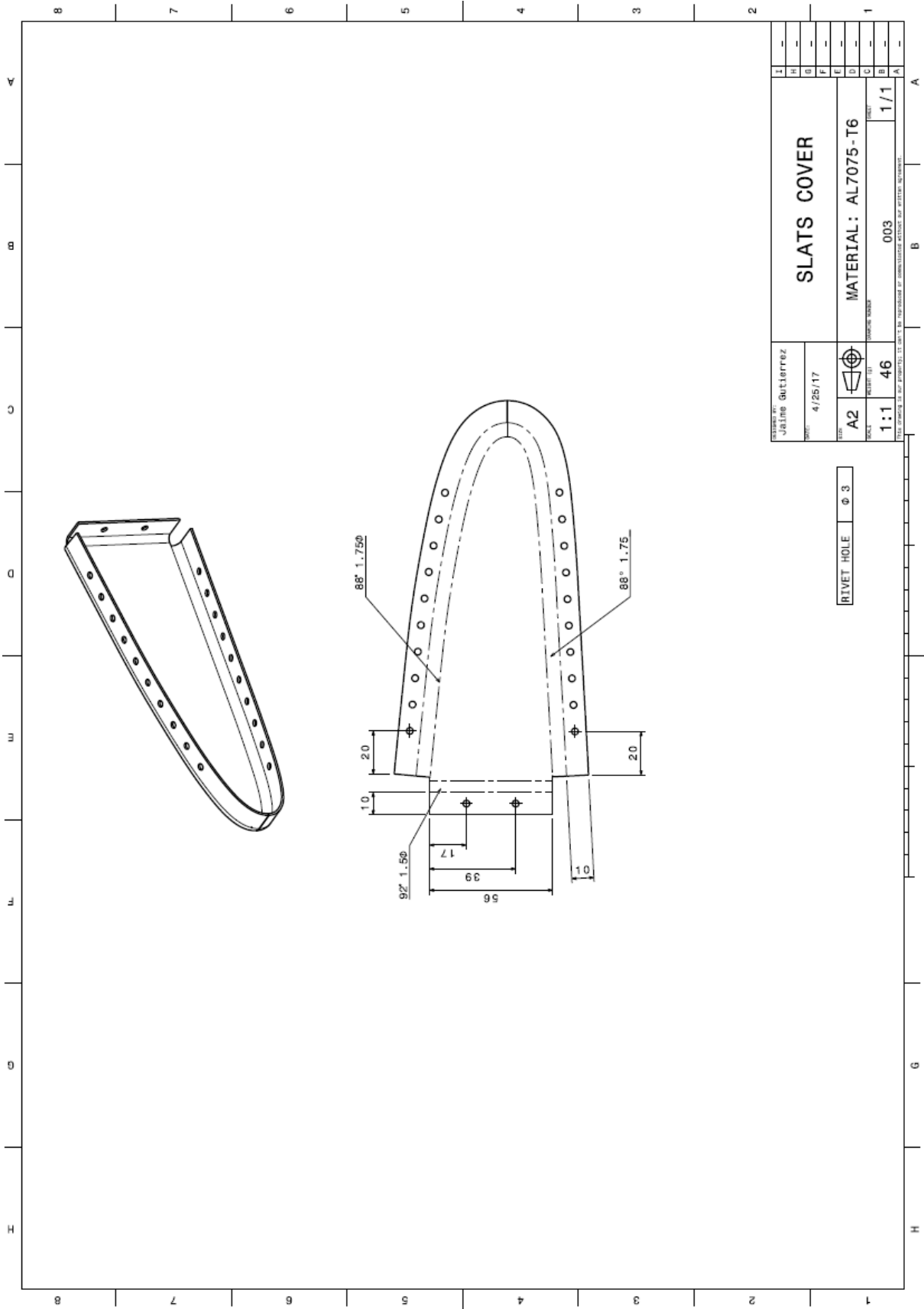


Figure A.4: Slat cover

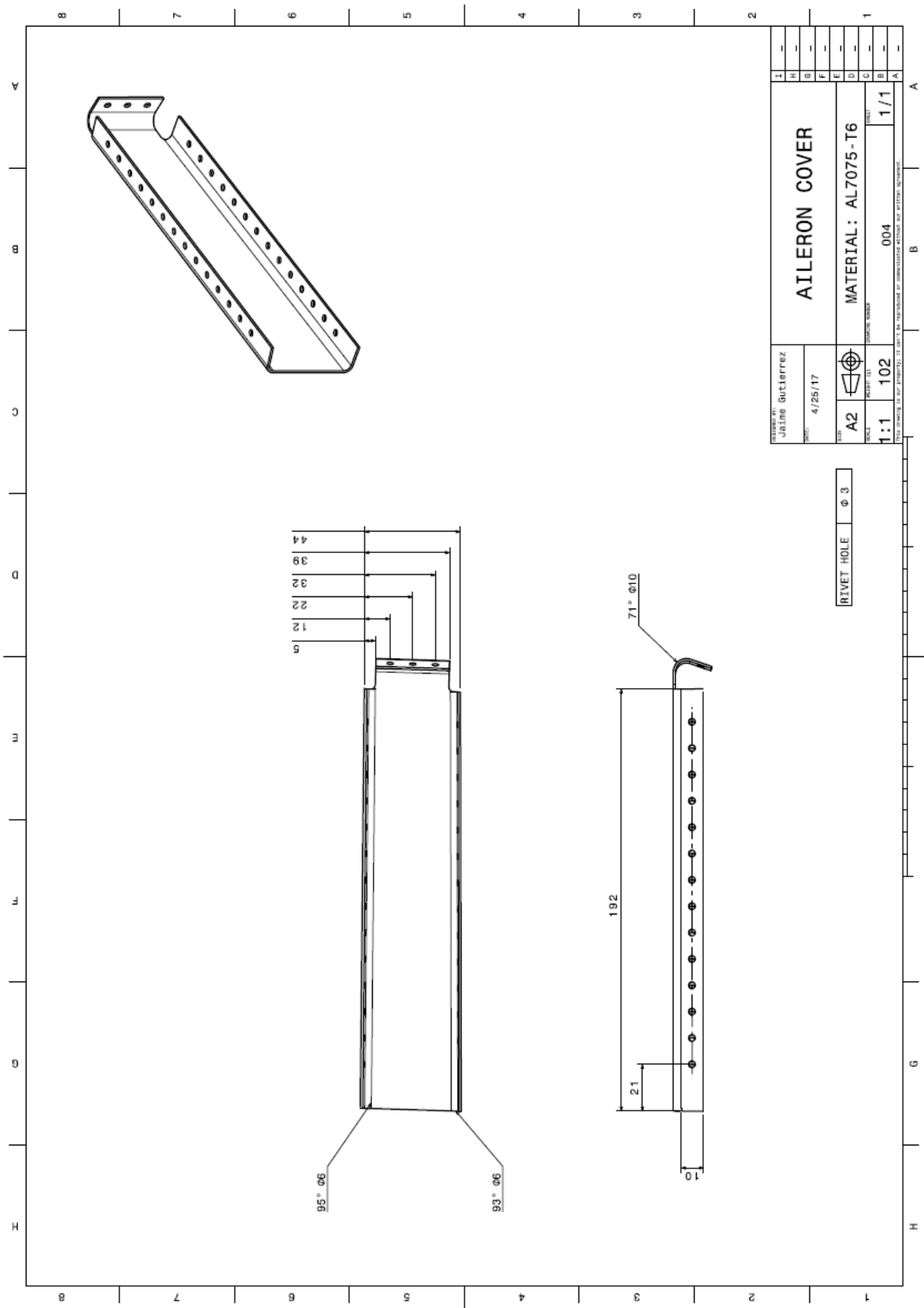


Figure A.5: Aileron cover

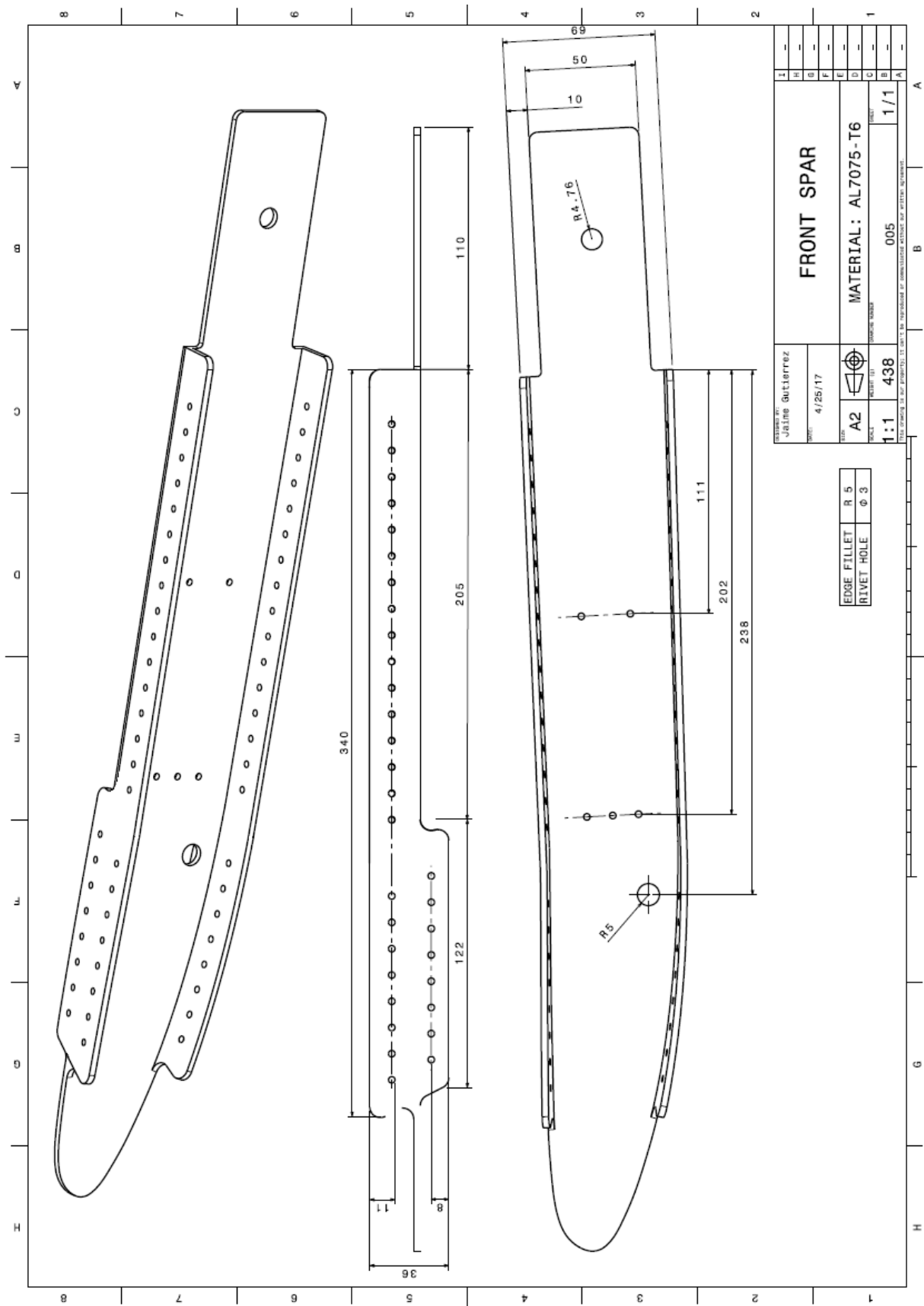


Figure A.6: Front spar

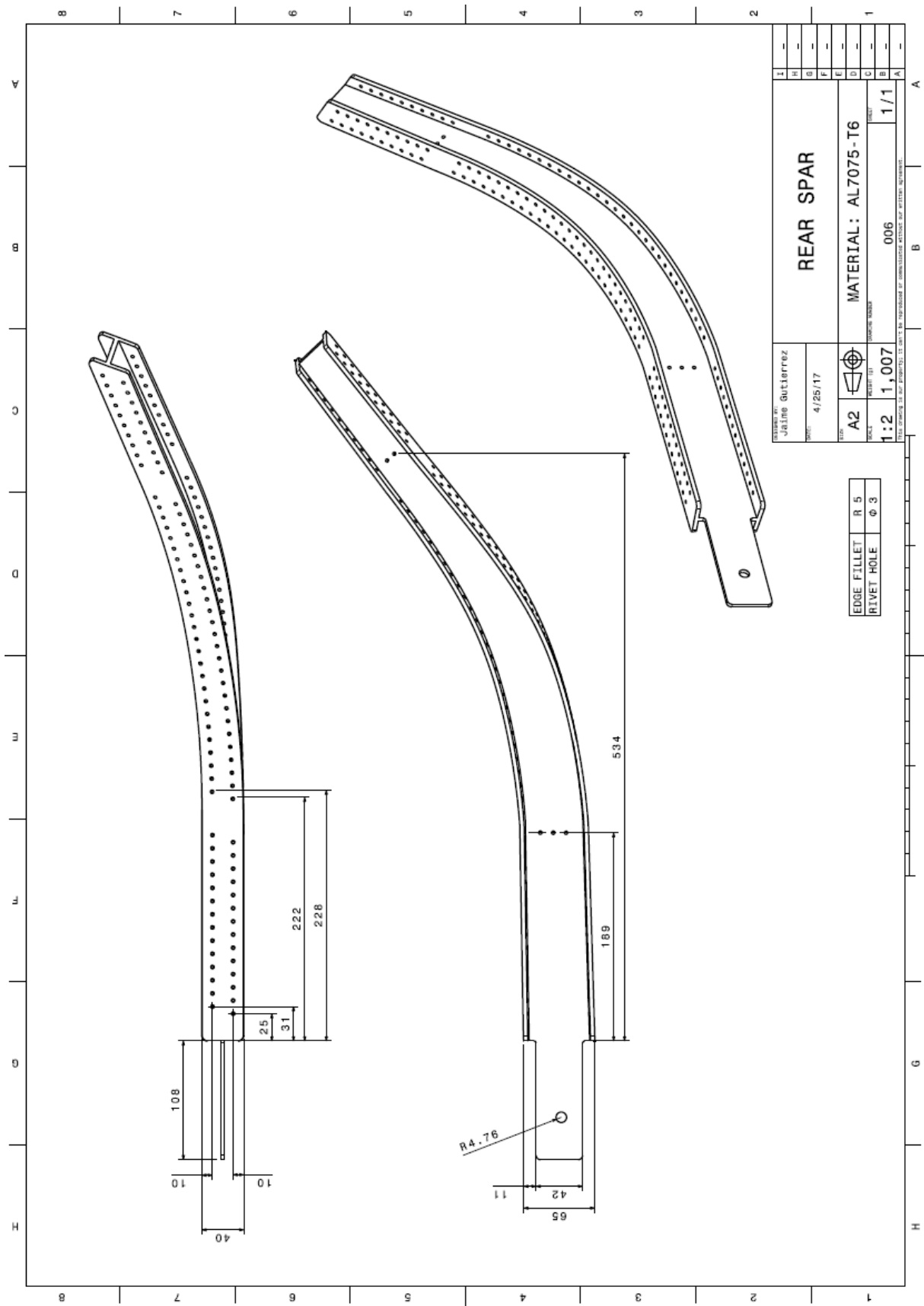


Figure A.7: Rear spar

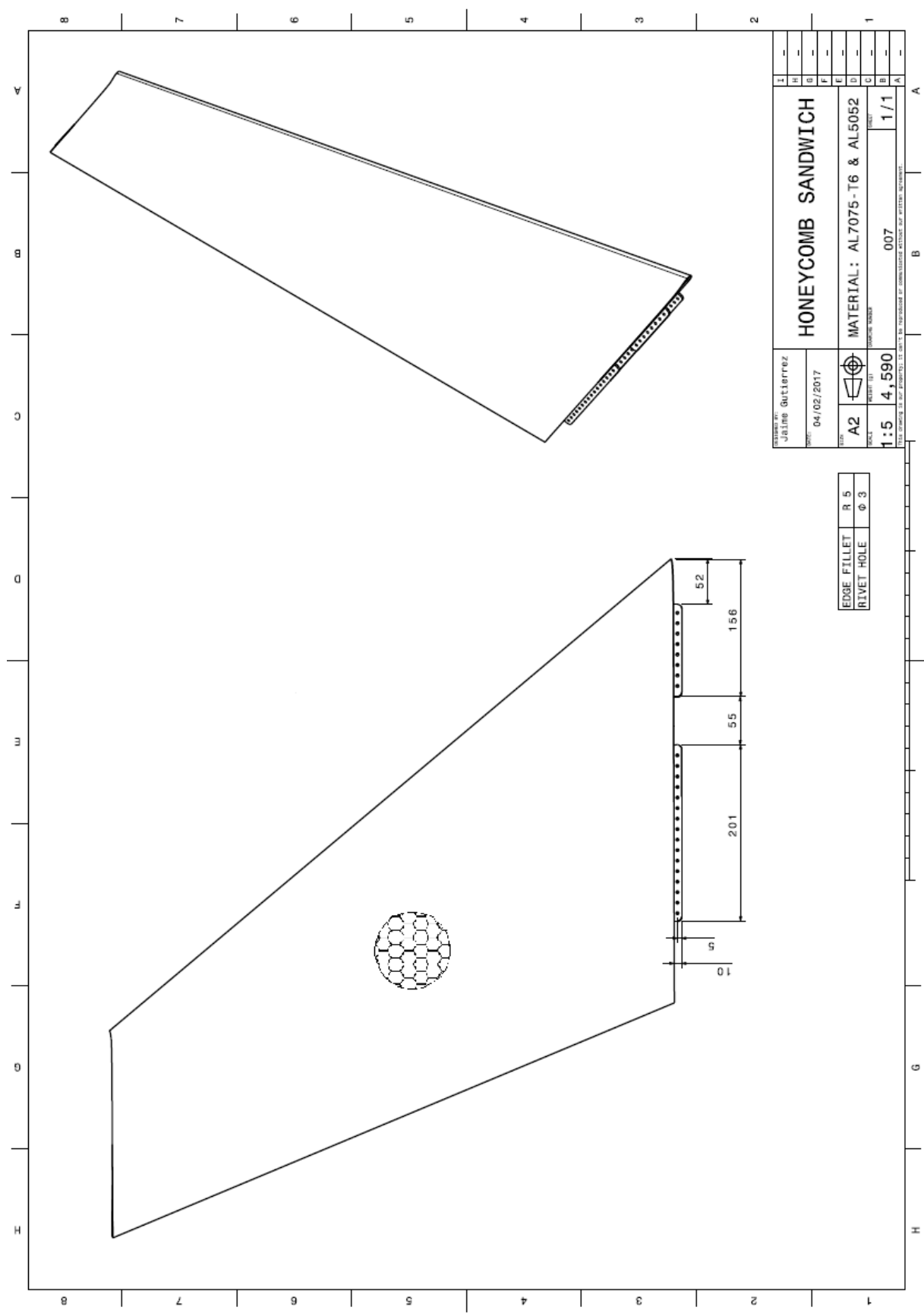


Figure A.8: Honeycomb sandwich

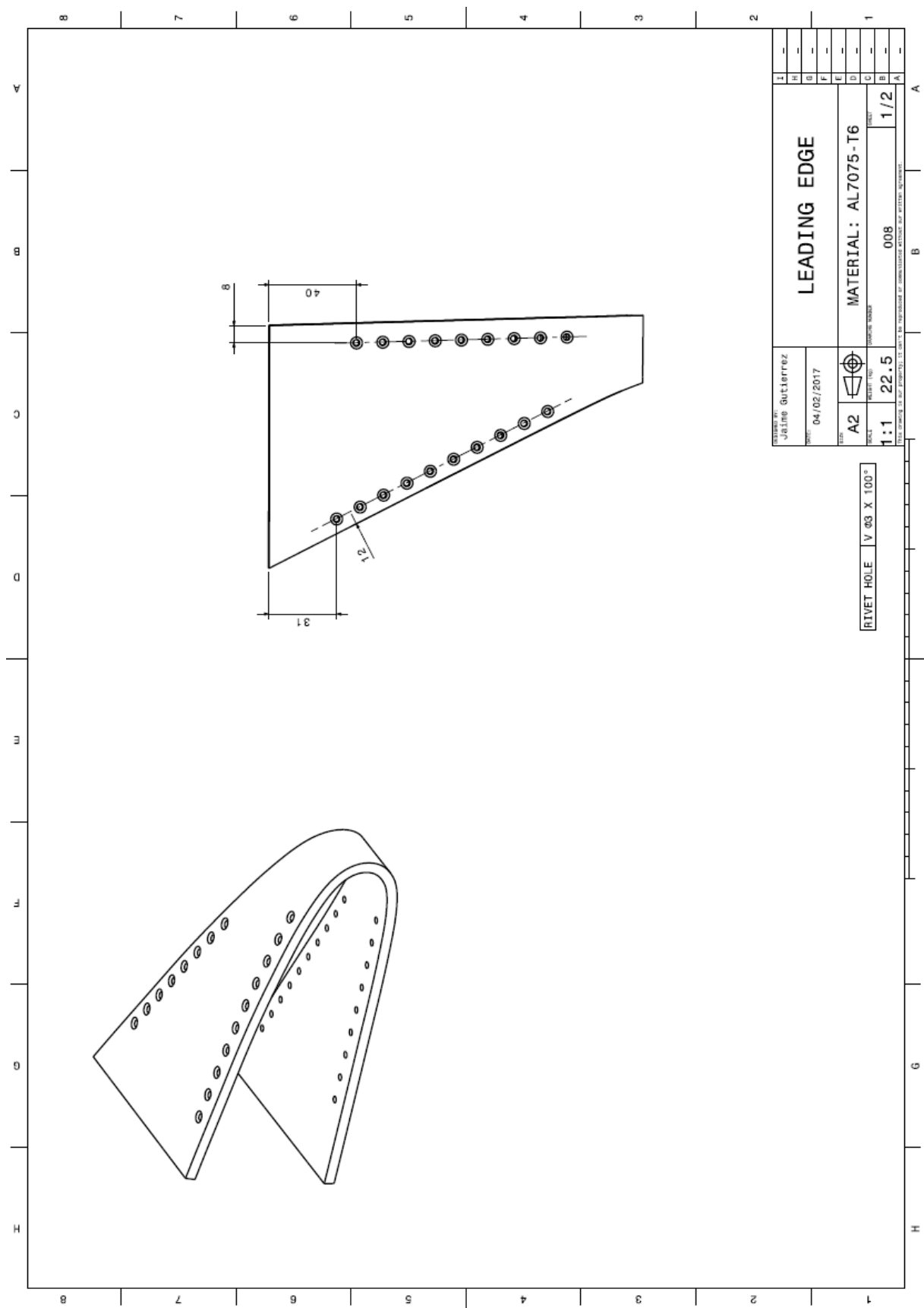


Figure A.9: Leading edge A

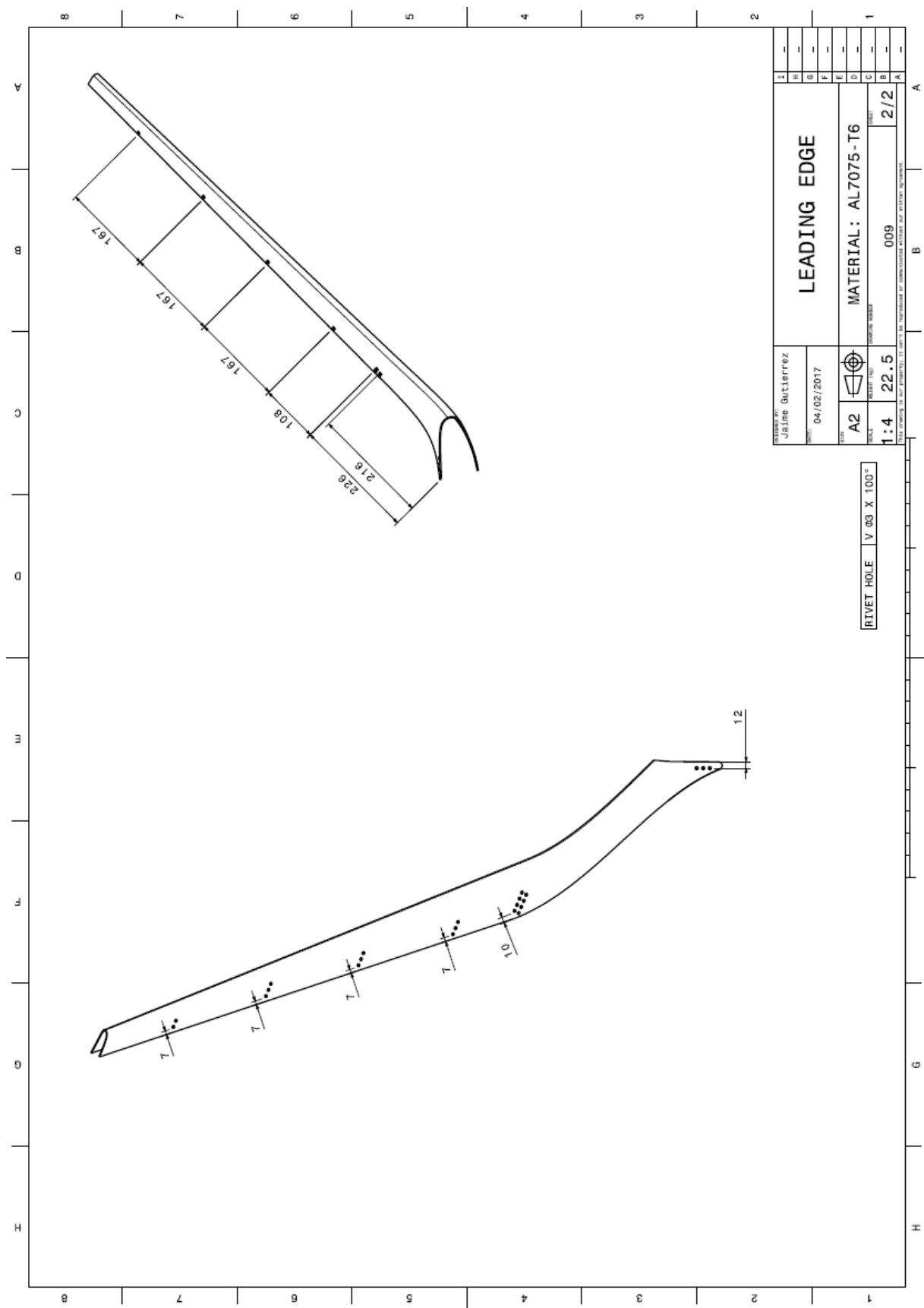


Figure A.10: Leading edge B

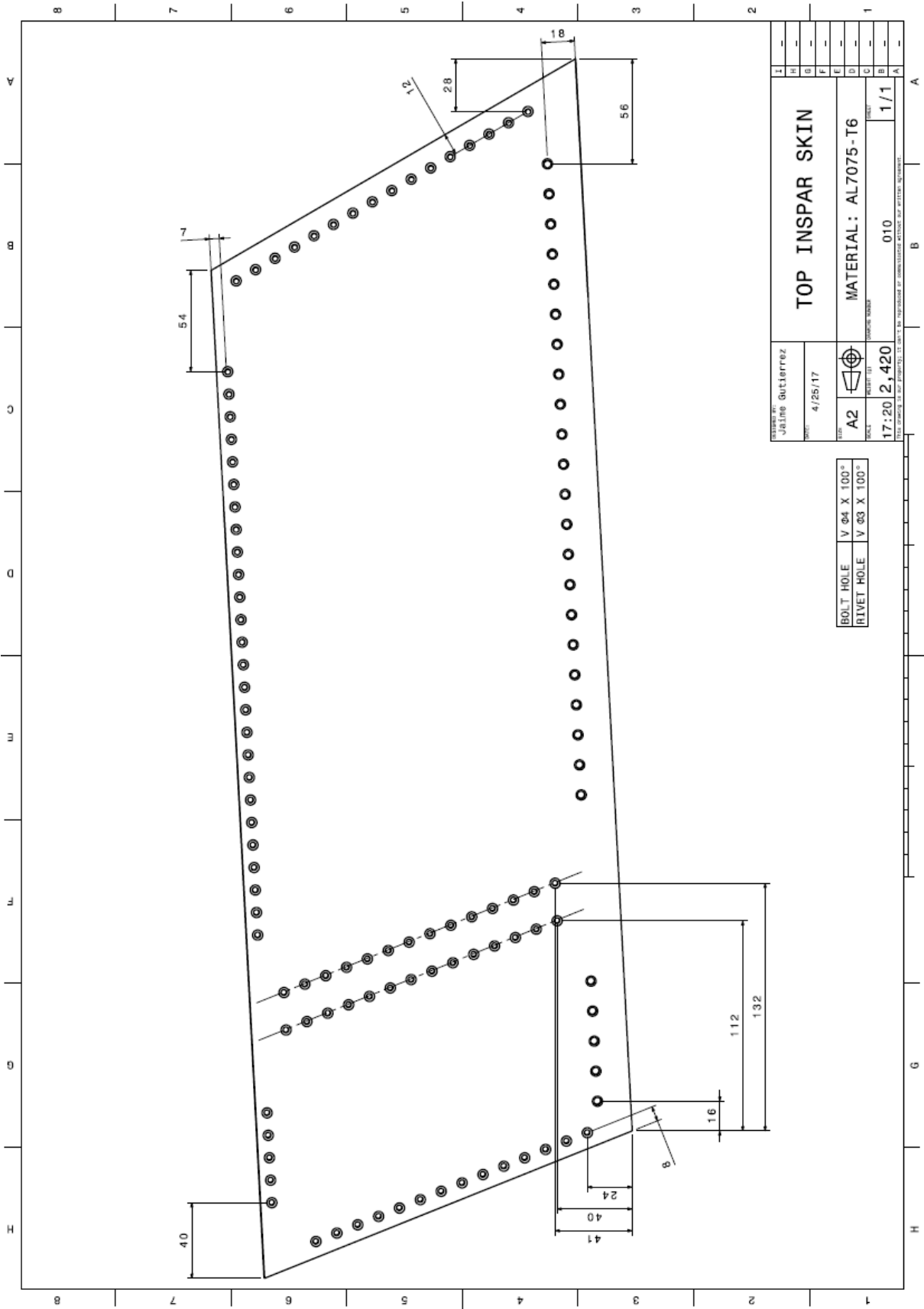


Figure A.11: Top inspar skin

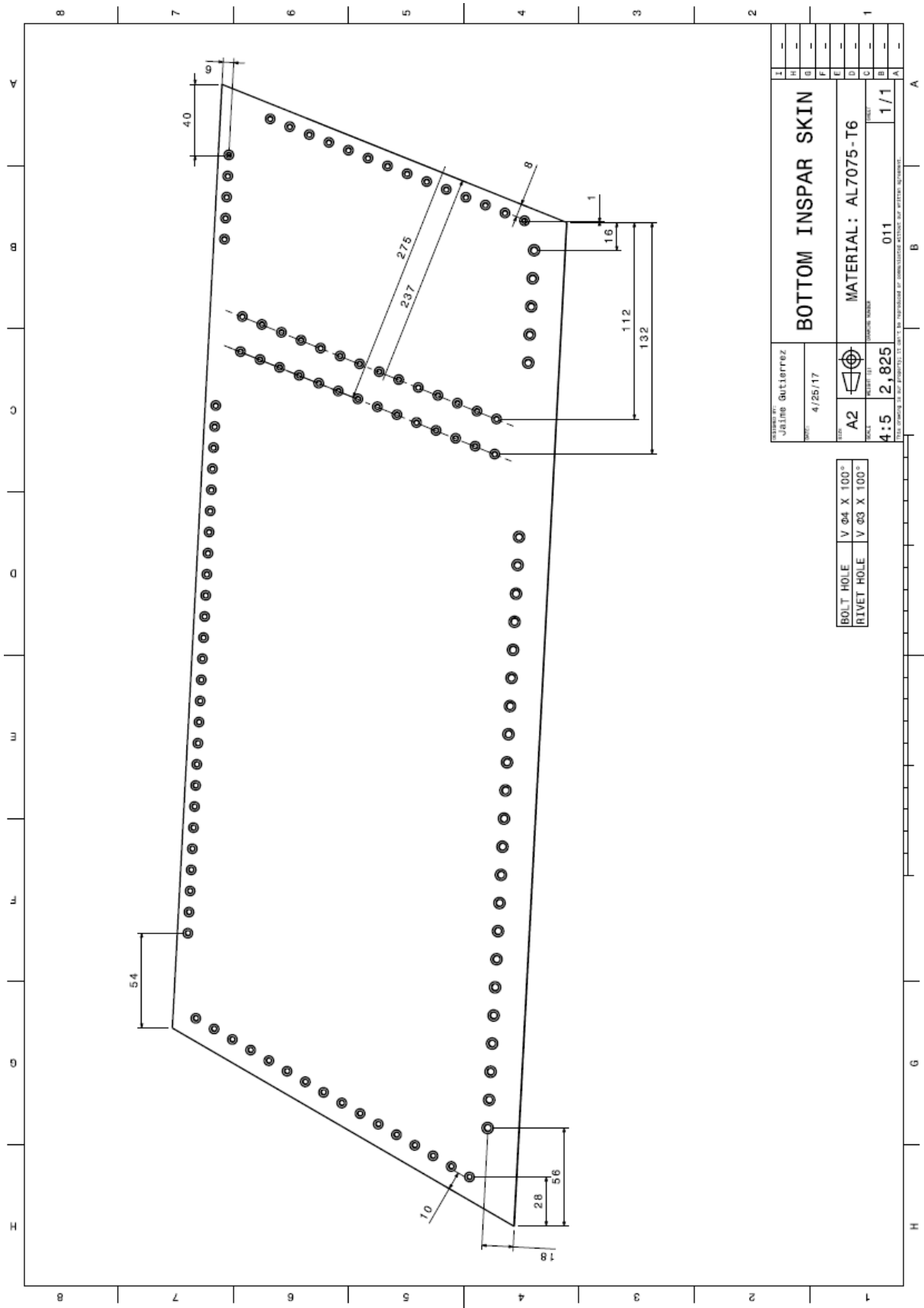


Figure A.12: Bottom inspar skin

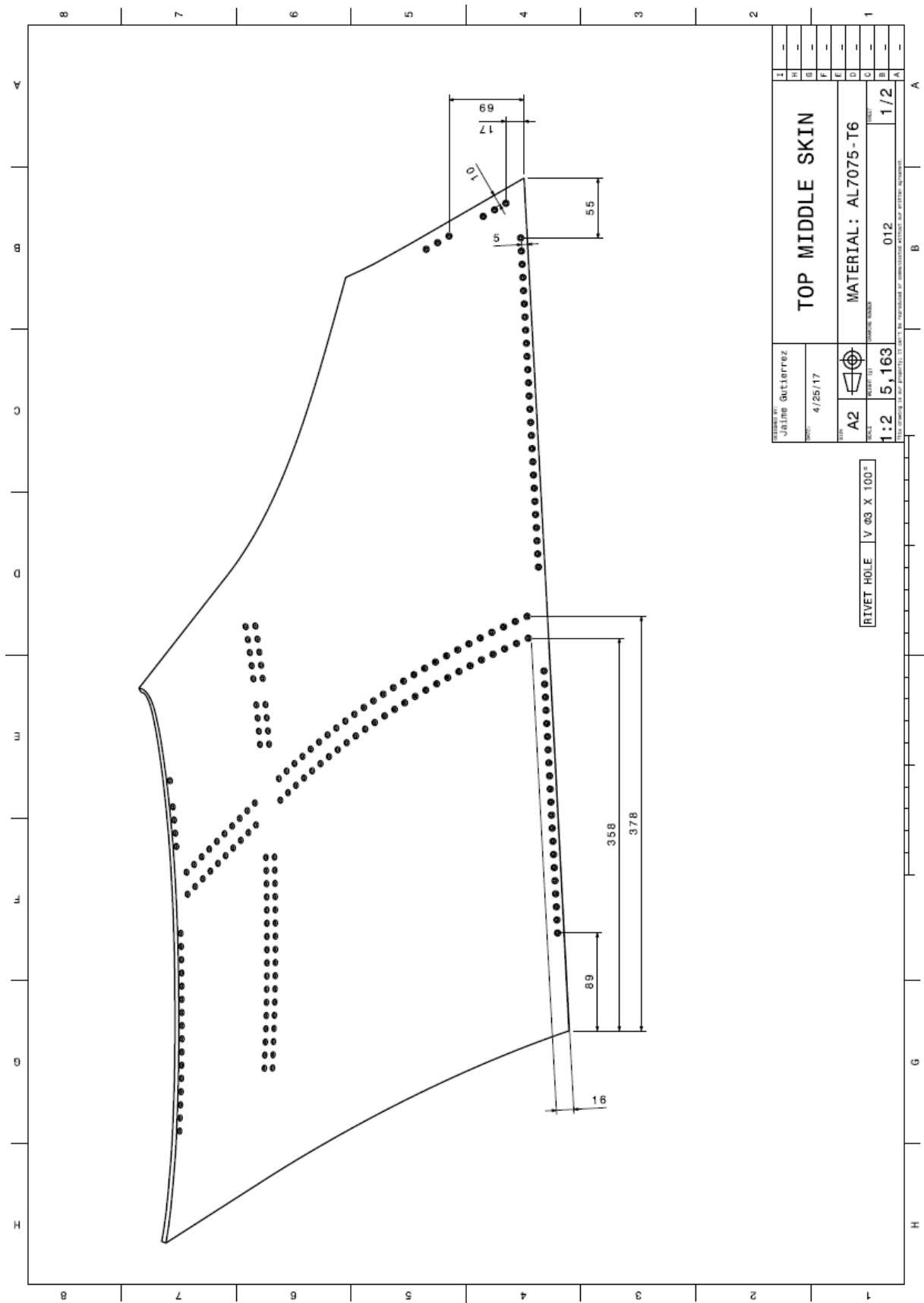


Figure A.13: Top middle skin

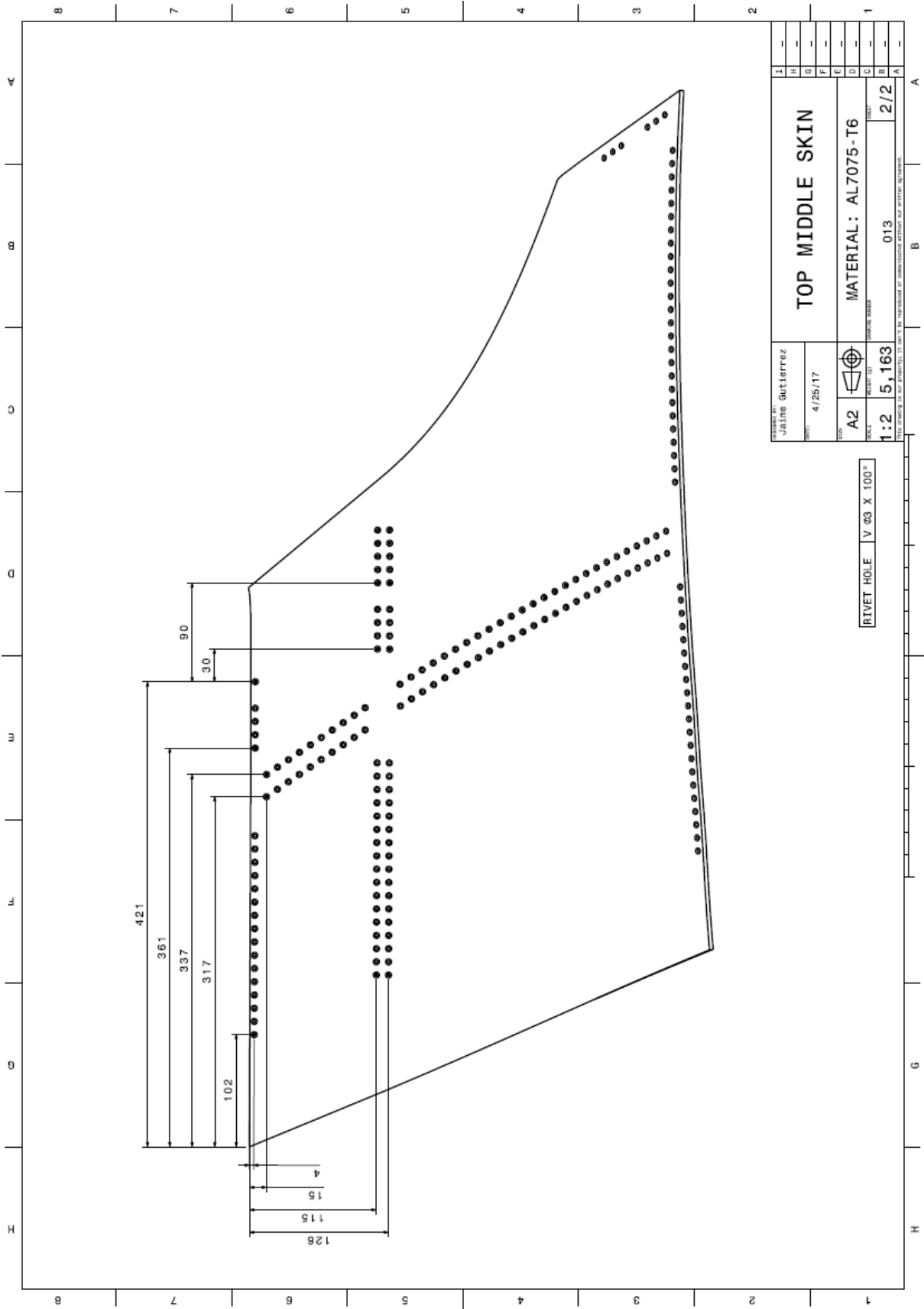


Figure A.14: Top middle skin

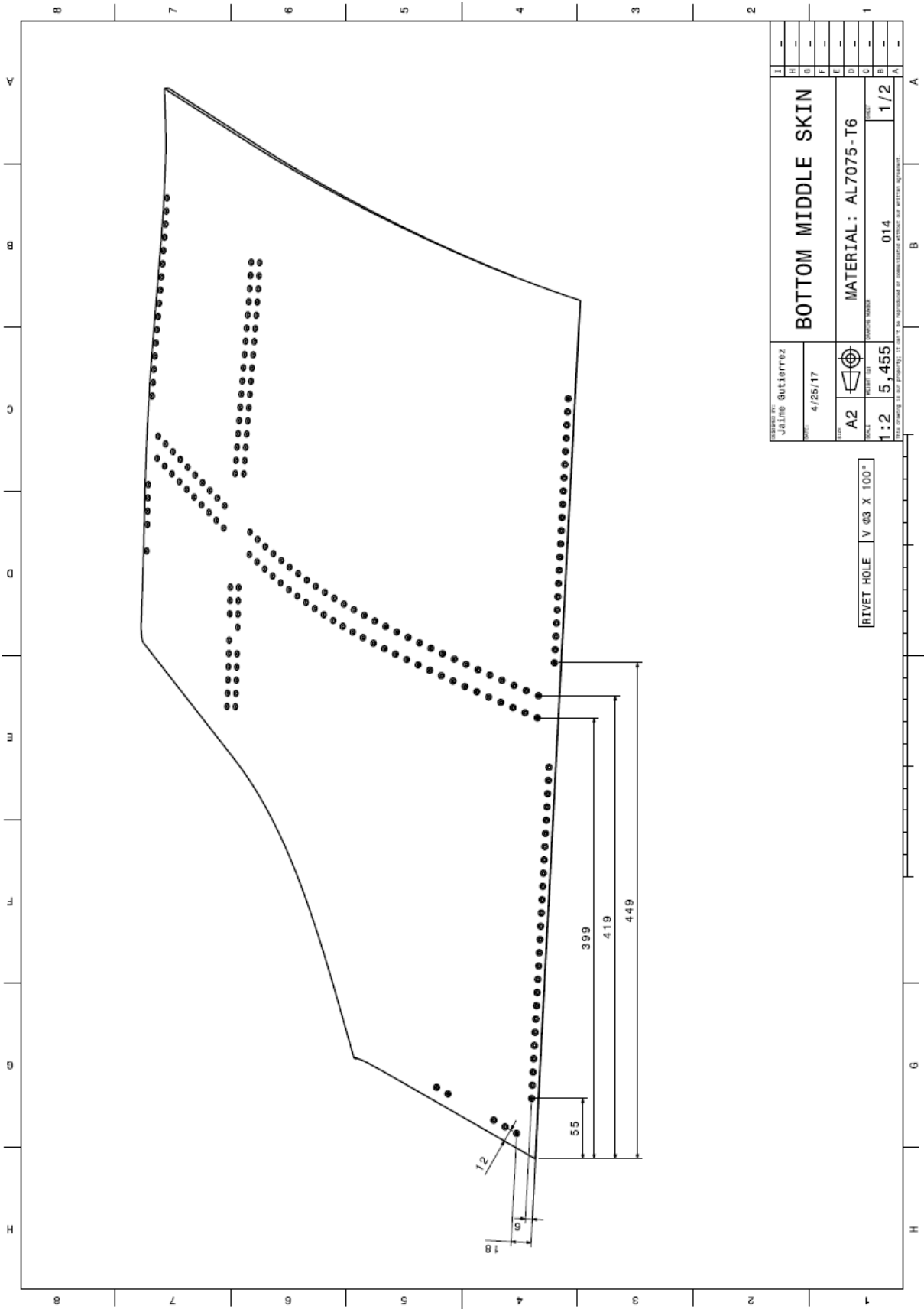


Figure A.15: Bottom middle skin

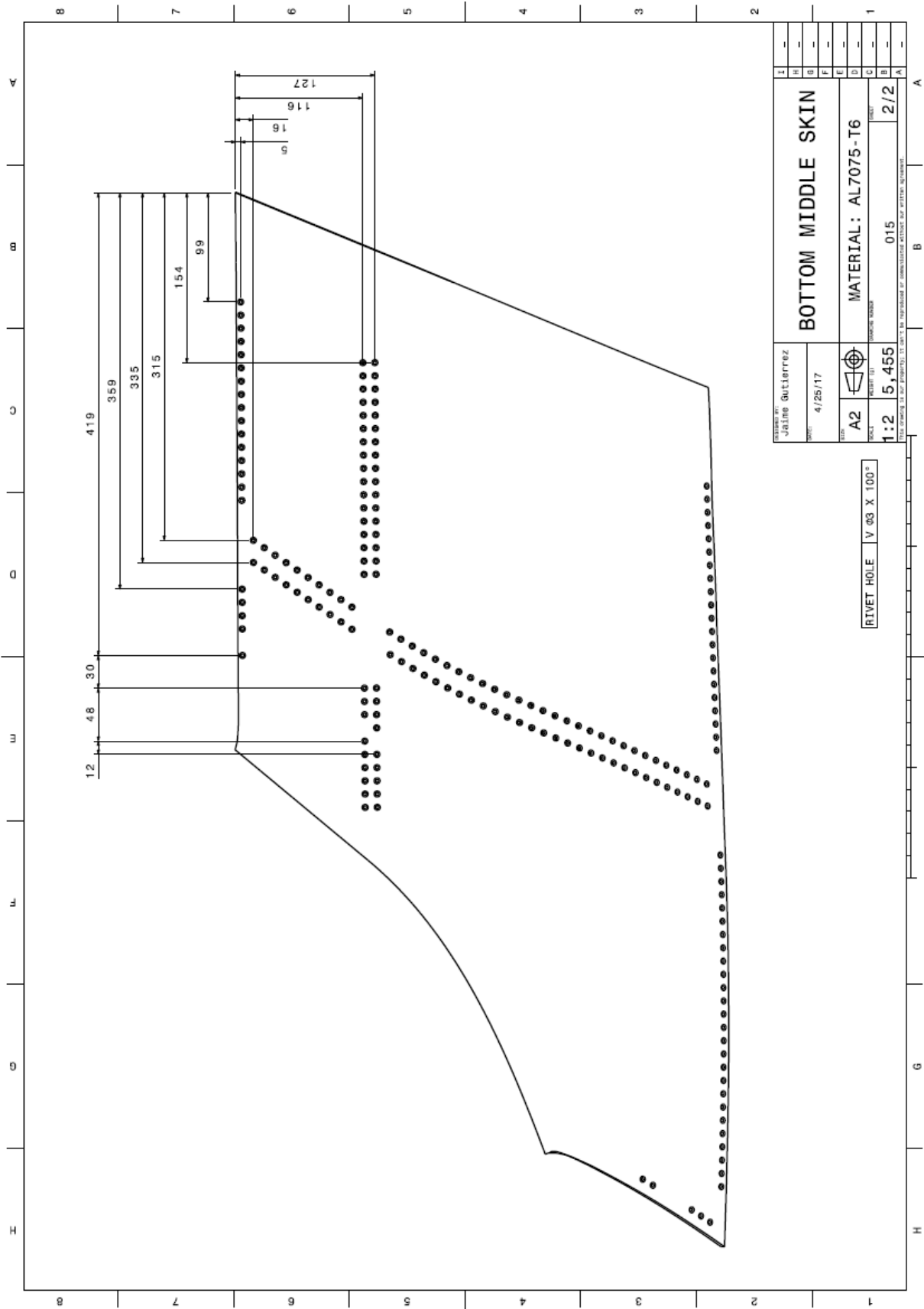


Figure A.16: Bottom middle skin

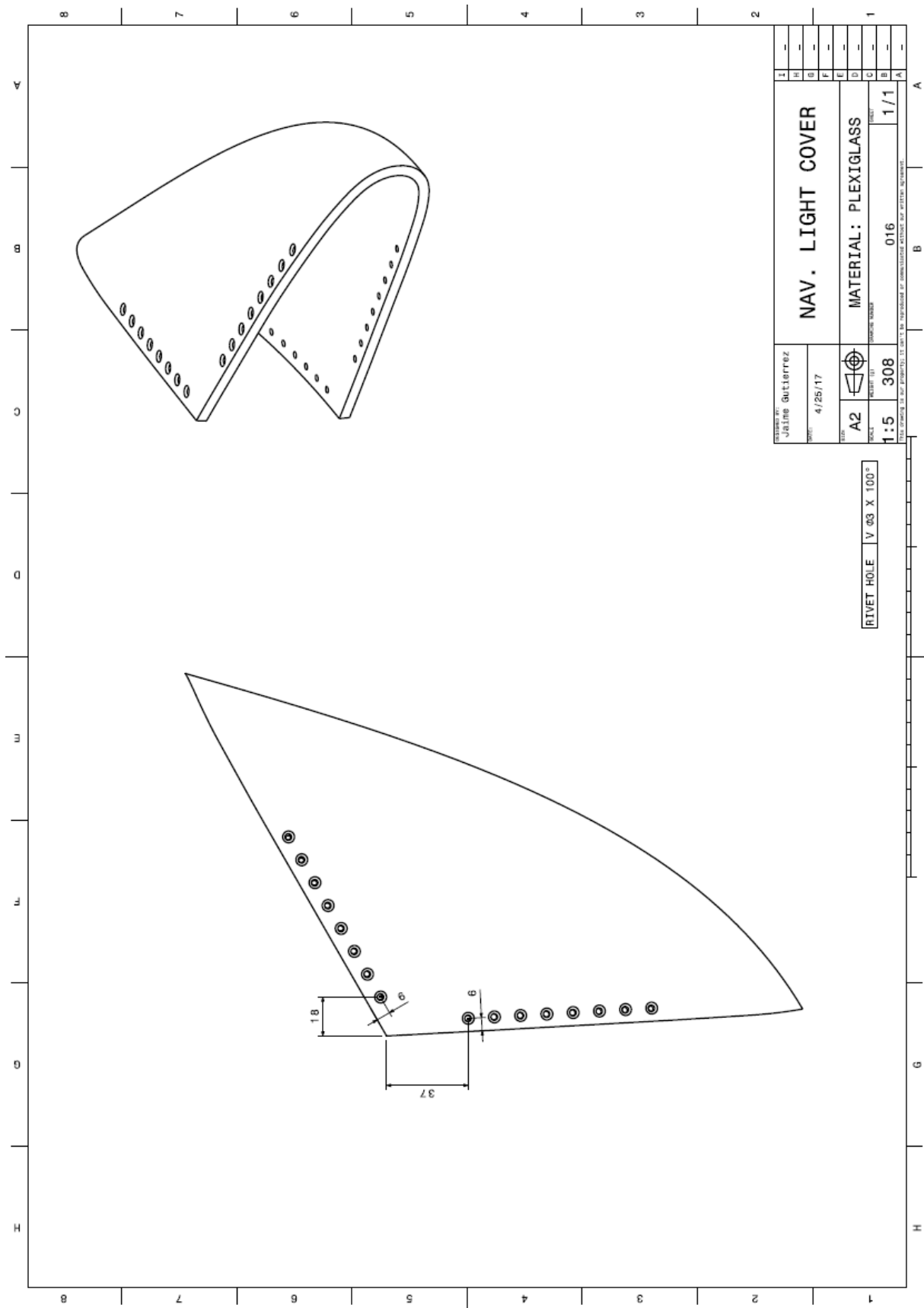


Figure A.17: Navigation light cover